

# 1 Near-surface characterization and delineation of water 2 preferential flow-pathways at South Deep Gold Mine, South 3 Africa

4 Sikelela Gomo<sup>1</sup>, Farbod Khosro Anjom<sup>2</sup>, Chiara Colombero<sup>2</sup>, Mohammadkarim Karimpour<sup>2</sup>, Bibi  
5 Ayesha Jogee<sup>1</sup>, Musa S.D. Manzi<sup>1</sup>, Laura V. Socco<sup>2,3</sup>

6 <sup>1</sup>School of Geosciences, University of the Witwatersrand, Johannesburg, Private Bag, Wits, 2050, Republic of South  
7 Africa.

8 <sup>2</sup>Department of Environment, Land and Infrastructure Engineering, Politecnico di Torino, Turin, 10129, Italy.

9 <sup>3</sup>Department of Geoscience and Engineering, Delft University of Technology, Delft.

10 *Correspondence to:* Sikelela Gomo (1488846@students.wits.ac.za)

11 **Abstract.** Velocity models of the shallow subsurface (a few hundred meters) are important in near-surface  
12 characterization, improving seismic mapping resolution at depth, and constraining deeper geological models. It is  
13 therefore interesting to retrieve them from deep seismic exploration data. We compute the near-surface shear wave  
14 velocity model in the vicinity of South Deep Gold Mine, using surface waves present in the small-offset 2D and 3D  
15 seismic reflection data acquired between 2022 and 2023 at the mine for research, mine planning, and development  
16 purposes. The obtained near-surface model is then used to (1) characterize the near-surface, and (2) better constrain  
17 the interpretation of possible water preferential flow-pathways (faults, fracture zones, and dykes) mapped at mining  
18 levels, that enable the migration of water from overlying aquifer systems (< 0.5 km depth) to the mining levels (~ 3  
19 km depth). The analysis is carried-out on reflection seismic data acquired for deep mineral exploration, where the  
20 acquisition parameters were not optimized for surface wave techniques and the reciprocity principle is used to improve  
21 the data density, coverage, and near-surface mapping resolution. The lithostructural information retrieved from the  
22 produced pseudo-2D and 3D shear wave velocity models is consistent with information obtained from available  
23 surface borehole data and published records in the study area. To investigate the structural linkage between the deep  
24 mining levels and shallow groundwater aquifers, we integrated the near-surface shear wave velocity model produced  
25 from the small-offset 2D and 3D reflection seismic data with the large-offset 2003 3D reflection seismic data, and  
26 geological structures derived from underground mapping, and exploration drilling. The shear wave velocity models  
27 help define the faults, fractures, and dykes that compartmentalize the near-surface groundwater aquifer systems. The  
28 large-offset legacy 2003 3D seismic data, underground mapping, and exploration drilling provide a better definition  
29 of the orebody and its offsets (e.g., faults) at the mining level. The integrated data show that several geological  
30 structures (e.g., faults and dykes), defined by legacy seismic data, underground drilling, and mapping, cross-cut the  
31 mining levels at ~ 3 km depth and intersect the near-surface aquifers, thus making these structures possible preferential  
32 flow-pathways for water migration to the deep mining levels. The results of the interpretation illustrate the advantages  
33 of integrating shallow and deep subsurface information to constrain the timing of geological events and mitigate the

34 risks associated with water ingress to the mining levels. The final model produced can be used for future mine  
35 development, improving safety and production, and for the extension of the Life of Mine (LoM).

36

## 37 **1 Introduction**

38 The Mesoarchean-aged Witwatersrand Basin hosts the largest known gold deposit in the world and has produced more  
39 gold than any other ore province globally (Frimmel, 2019). Seismic techniques have been used extensively in the  
40 exploration of the Witwatersrand Basin, mainly for mapping and evaluating gold-bearing quartz pebble conglomerates  
41 (locally termed ‘reefs’) for mining purposes (i.e., planning, production, and risk mitigation) and for imaging faults  
42 and dykes. Seismic imaging of faults and dykes, in particular, is important in deep underground gold mines as these  
43 structures might (1) act as possible preferential flow-pathways for water and methane migration into the mining levels,  
44 (2) cross-cut the orebody and make it impractical to mine (Campbell and Crotty, 1988; Pretorius et al., 1989; Gibson,  
45 2005; Manzi et al., 2012a), and (3) cause damaging seismic events (Masethe et al., 2023). The first 3D application of  
46 seismic techniques in hard-rock mining environments, particularly for mineral exploration, trace back to the surveys  
47 conducted by Campbell and Cotty (1988, 1990) at South Deep Gold Mine in 1986 in the Witwatersrand Basin.  
48 Campbell and Crotty (1990) applied active-source surface 3D seismic surveys to image the gold-bearing horizons and  
49 geological structures at depths down to 3.5 km below ground surface. This pilot study investigated and demonstrated  
50 the potential that the 3D seismic technique has in hard-rock environment for mineral exploration. In 2003, Gold Fields  
51 commissioned one of the largest 3D seismic surveys in the Witwatersrand basin to map the deep-seated gold deposits  
52 (e.g., Ventersdorp Contact Reef, VCR) and subsurface geological structures (e.g., faults and dykes) across its Kloof  
53 and South Deep gold mines for mine planning purposes (Manzi et al., 2012a). The legacy 2003 Kloof-South Deep  
54 Gold Mine data have been the subject of several studies over the past 20 years, given the size of the survey area and  
55 the unique nature of the data, particularly the strong seismic reflections associated with deep-seated gold-bearing  
56 horizons and the delineation of complex geological structures that cross-cut the gold deposits (Manzi et al., 2012a,b;  
57 Manzi et al., 2013a,b). The data have also been used by Manzi et al. (2012b) to map potential conduits of water and  
58 methane at deep mining levels of the Kloof Gold Mine. They have been used to constrain Neoproterozoic tectonic history  
59 and the ore genetic models in the Witwatersrand basin (Manzi et al., 2013b; Malehmir et al., 2014).

60 Between 2022 and 2023, high-resolution 2D and 3D deep seismic reflection (DSR) surveys were conducted at South  
61 Deep Gold Mine as part of the ERA-MIN3 Future project (Rapetsoa et al., 2025). The work mainly focused on testing  
62 the modern seismic technologies to image the deep (~ 3 km) gold-bearing horizons such as the Ventersdorp Contact  
63 Reef (VCR), Upper Elsburg Reefs (UER), and complex geological structures (e.g., faults and dykes) that cross-cut the  
64 orebodies. The seismic surveys used a seismic nodal system incorporating one vertical and three component recorders  
65 connected to 5 Hz geophones, broadband micro-electromechanical system (MEMS) accelerometers, distributed  
66 acoustic sensing technology, and a 6-ton broadband (2-200 Hz) seismic vibrator operating with sweep lengths between  
67 24s and 48s (Rapetsoa et al., 2025). In this work, we utilize the surface waves (SWs) present in the DSR survey data  
68 acquired at the mine to estimate the near-surface shear-wave (S-wave) velocity model in the vicinity of the mine,  
69 which is used to better understand the near-surface stratigraphic (lithological) and structural (e.g., faults and dykes)

70 geological variations in the study area. We then integrate the near-surface S-wave velocity model with the 2003 legacy  
71 seismic data and mine geological structures to investigate the structural linkage between shallow geology (aquifers)  
72 and deep mining levels, where the orebody is located, to constrain the timing of structural activities and determine  
73 potential preferential flow-pathways for water ingress into the mining levels.

74 The near-surface is a geologically complex environment, often consisting of heterogeneous structures characterized  
75 by highly weathered and diverse materials, i.e., that may vary from loose, fractured, to solid rocks, which have the  
76 potential to significantly obscure the ability to resolve deeper lying seismic targets (Sheriff, 2002; Zhou et al., 2010;  
77 Strong, 2018). Near-surface characterization is an essential process in exploration, mining, engineering, and  
78 environmental studies as it can provide information that can be used to improve the imaging of deeper lying geological  
79 structures, conduct risk assessments, efficiently plan projects, and design and construct safer and better-performing  
80 mining, environmental, and civil engineering infrastructures (Laake et al., 2008; Zhu et al., 2008; Socco et al., 2010;  
81 Pegah and Liu, 2016; Papadopoulou et al., 2020). The application of seismic surface wave (SW) analysis to determine  
82 near-surface velocity models at hard-rock sites is limited due to the challenge of obtaining good-quality data (Socco  
83 et al., 2019; Papadopoulou et al., 2020; Wilczynski et al., 2025). The quality of SW data at hard-rock mining sites can  
84 be severely affected by (1) the presence of lateral heterogeneities (e.g., dykes, fractures, and faults) which can generate  
85 scattering and back reflections (Pileggi et al., 2011; Malehmir et al., 2015); (2) noise generated by mining activity  
86 (e.g., blasting, excavations, drilling, crushing, moving heavy machinery, and mining operations) (Urosevic et al., 2007;  
87 Grszczyk et al., 2015); and (3) variable and extreme near-surface conditions caused by the presence of hard and rugged  
88 topography, roads, areas of outcropping hard rocks, and the presence of swampy soils or dense vegetation (Saunders  
89 et al., 1991; Eaton et al., 2003; Heinonen et al., 2011; Malehmir et al., 2017). However, the dominance of SWs in  
90 seismic records, their high sensitivity to near-surface properties, their ability to resolve low-velocity zones or soft  
91 layers bounded by high-velocity materials, and their ability to avoid the water-masking effect in saturated media, make  
92 them a powerful tool for near-surface imaging (Foti et al., 2002; Socco and Strobbia, 2004).

93 This paper presents the application, potential, and benefits of conducting SW analysis to reflection seismic data mainly  
94 acquired for deep targeting in a mining environment. Multichannel analysis of surface wave (MASW) and the  
95 Laterally Constrained Inversion (LCI) are applied to high-resolution 2D and 3D seismic data to estimate the near-  
96 surface S-wave velocity model within the top ~ 300 m in the vicinity of South Deep Gold Mine. Since the deep  
97 exploration data acquired at the mine are not optimized for SW analysis (i.e., characterized by coarse spatial sampling)  
98 and are therefore not ideal for SW analysis, we utilize the reciprocity theorem to extract all the possible information  
99 in the data, and increase the data coverage by providing a grid of orthogonal sets of dispersion curves along receiver  
100 and source lines. Comparison with available borehole data in the vicinity of the mine indicates that the conducted  
101 analysis is sensitive to stratigraphic and structural variations beneath the acquired DSR surveys and resolves them  
102 quite well with depth. Lastly, we integrate the obtained near-surface S-wave velocity model with existing and available  
103 legacy 2003 active-source P-wave seismic reflection data, mine mapping, and drilling information to investigate the  
104 structural continuity and connectivity between the shallow aquifers (< 0.5 km) and deep mining levels (~ 3 km). These  
105 mine-mapped structures are well known in the Witwatersrand gold mines (e.g., South Deep Gold Mine and Kloof

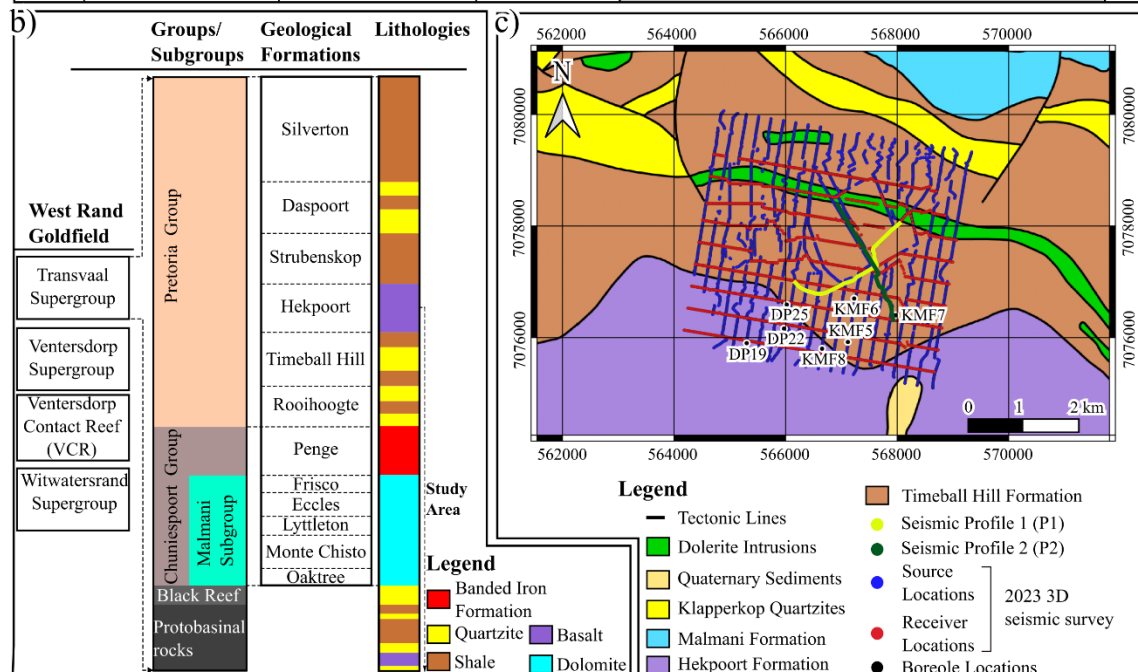
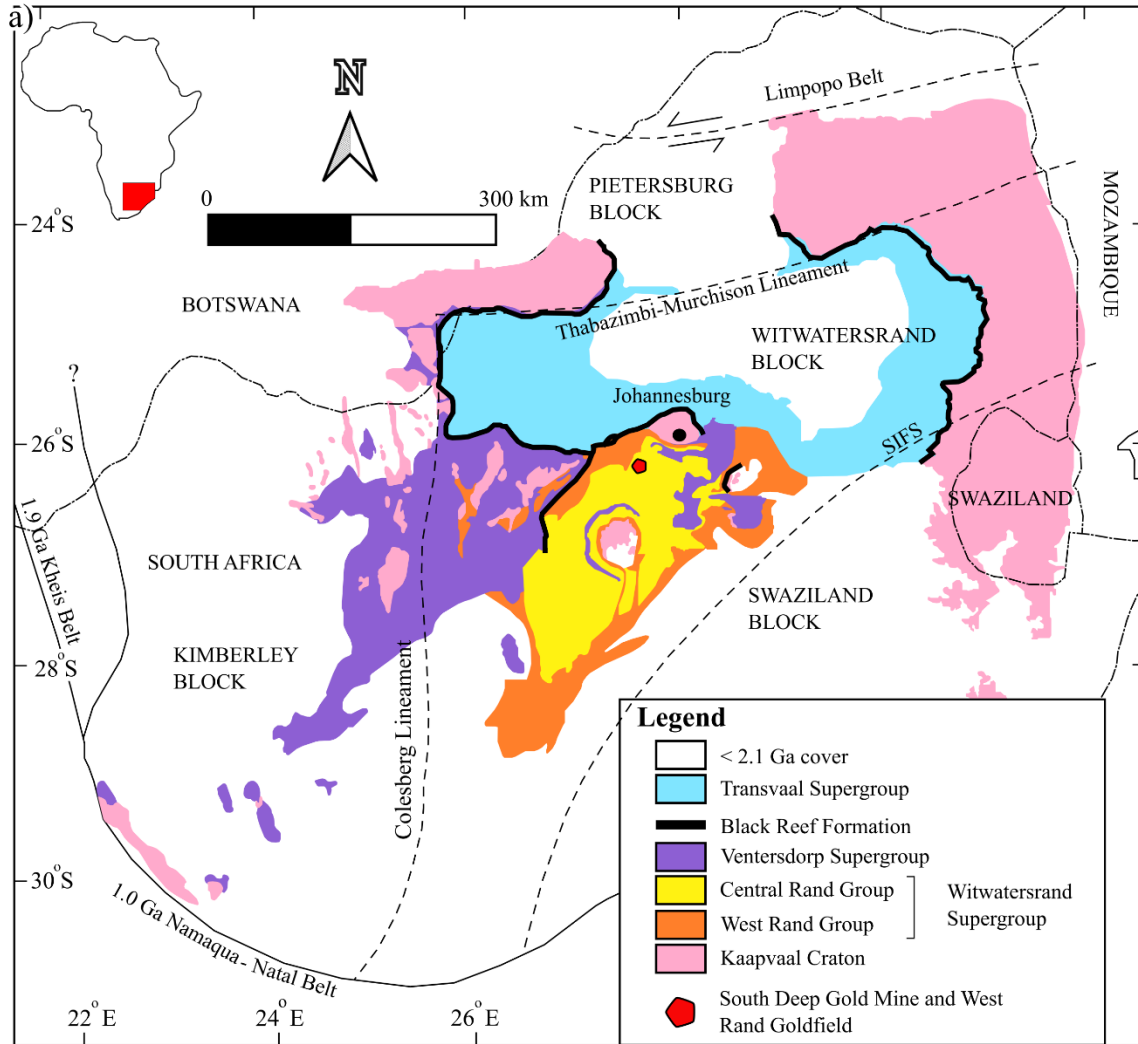
106 Gold Mine) to be associated with mining-induced seismicity, water migration, and methane gas pockets (Manzi et al.,  
107 2012b; Masethe et al., 2023). The existing large-offset legacy 2003 3D seismic data provides high-resolution imaging  
108 of subsurface geological structures from 0.5 km up to 6 km below the ground surface. The integration of the near-  
109 surface S-wave model with the large-offset legacy 3D seismic data, underground mapping, and drilling information  
110 enabled the tracking (vertically) of these structures through the thick 3 km strata from their known positions at the  
111 mining levels to the near-surface. Thus, these different methods and datasets were integrated to overcome their  
112 inherent limitations and leverage their strengths.

113 In this paper, we (1) describe the mining site and its geological setting, (2) present the seismic data acquisition  
114 parameters and the characteristics of the data, and outline the processing and inversion strategy, and (3) discuss the  
115 obtained velocity models in connection with surface borehole data, underground mine-mapped structures, and legacy  
116 deep seismic data.

117

## 118 **2 Site and data**

119 South Deep Gold Mine is situated southwest of the city of Johannesburg, in the southern portion of the West Rand  
120 Goldfield and on the northern margin of the Witwatersrand Basin (Fig. 1a). Excluding the Archaean granite-greenstone  
121 terrains (basement rocks) of the Kaapvaal Craton and basaltic-rhyolitic lavas and siliciclastic metasedimentary unit of  
122 the Dominion Group that underly the rocks of the Witwatersrand Supergroup, constituting the general setting in the  
123 West Rand Goldfield are the rocks of the, from oldest to youngest, Witwatersrand, Ventersdorp, and Transvaal  
124 Supergroups (Kositcin and Krape, 2004). The rocks of the Ventersdorp Supergroup are unconformably overlain by  
125 the Black Reef quartzite formation of the Chuniespoort Group belonging to the late Archean to early Proterozoic  
126 Transvaal Supergroup (Fig. 1b; Martin et al., 1998). The Transvaal Supergroup is a thick succession of chemical and  
127 sedimentary rocks, hosting well-preserved volcanic and glaciogenic units (Eriksson et al., 1993b; Bekker et al., 2014;) and  
128 world-class iron (Fe) and manganese (Mn) ores (Bekker et al., 2014; Smith and Beukes, 2016; Franchi, 2018) and  
129 comprises of the lower Chuniespoort and upper Pretoria Groups (Martin et al., 1998). The Chuniespoort Group  
130 dolomites consist of karst systems rich in water, which is primarily responsible for water inflow and inrush into mine  
131 shafts and mining levels (Van Niekerk and Van Der Walt, 2006).

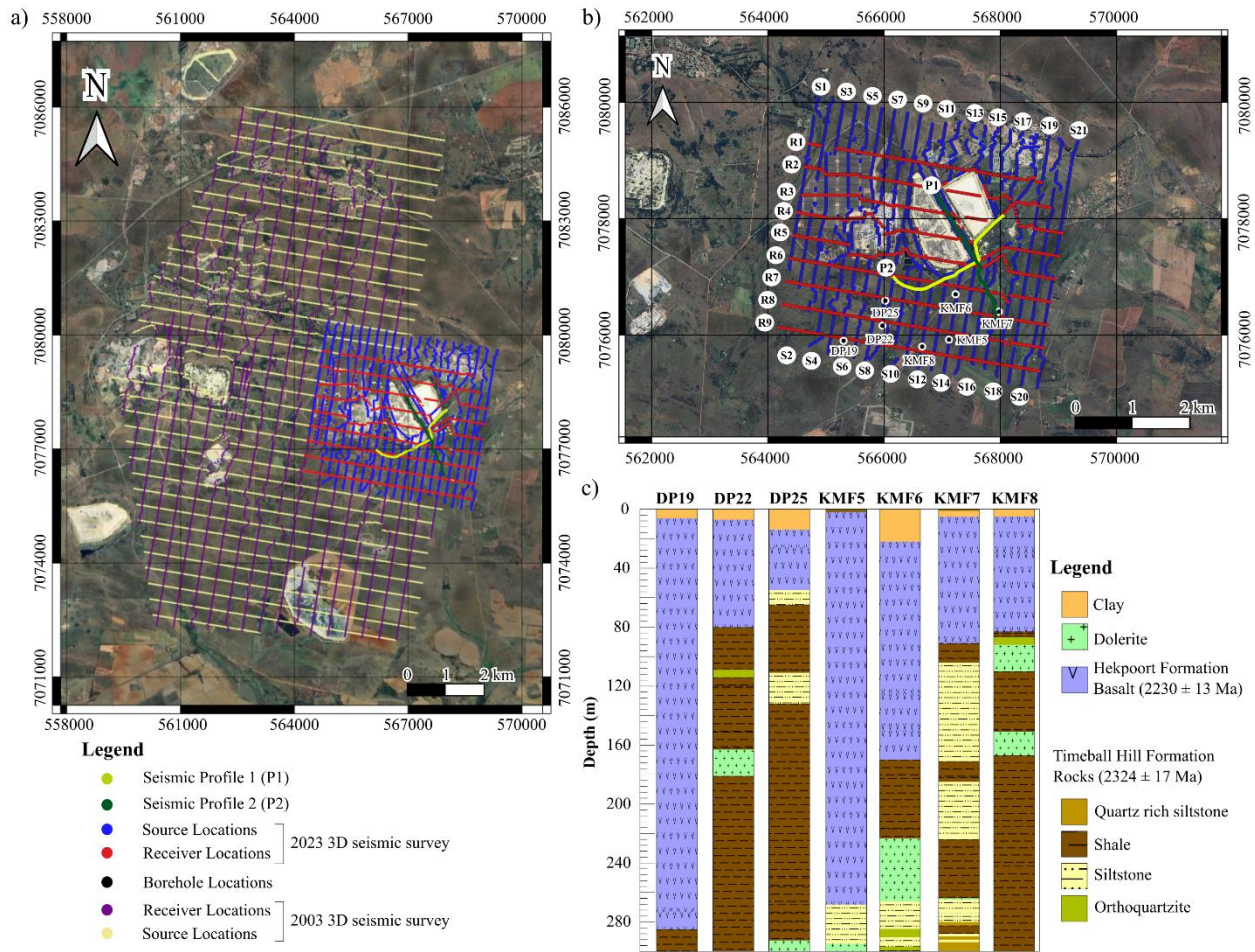


133 **Figure 1: (a) Simplified geological map showing both surface and subsurface distribution of the main Archaean**  
134 **stratigraphic units of the Kaapvaal Craton. The map shows the distributions of the Witwatersrand (comprised of the West**  
135 **Rand and Central Rand Groups), Ventersdorp, and the Transvaal Supergroups (modified after Frimmel, 2014). (b)**  
136 **Generalized stratigraphic column of the uppermost rocks in the Transvaal Supergroup, indicating the uppermost rock**  
137 **units outcropping in the study area. (c) A simplified geological map of the study area showing the locations of the high-**  
138 **resolution 2D profiles (P1- dark green and P2-yellow), and the receiver (red) and source (dark blue) lines of the 2023 3D**  
139 **seismic survey acquired in the vicinity of the mine. The map is plotted using the WGS 1984 UTM Zone 35S coordinate**  
140 **system. SIFS is the Saddleback-Inyoka Fault System.**

141

142 Predominantly outcropping in the vicinity of South Deep Gold Mine are the rocks of the Pretoria Group (2350 Ma-  
143 2250 Ma; Walraven et al., 1990; Martin et al., 1998). The Pretoria Group forms the upper part of the Transvaal  
144 Supergroup and primarily consists of a succession of shales, quartzose and arkosic sandstones, and significantly  
145 interbedded basaltic-andesitic volcanic rocks, and subordinate conglomerates, diamictites, and carbonate rocks  
146 (Killick, 1992; McCarthy, 2006). In the northern portion of the South Deep Gold Mine, rocks of the Malmani  
147 Subgroup, Timeball Hill Formation, and Klapperkop Quartzites are present, while south of the mine, outcrops of  
148 basaltic lava and tuff of the Hekpoort Formation exist (Fig. 1c; Osburn et al., 2014). Figure 2a and b show the locations  
149 of the legacy, large-offset 2003 and 2022-2023 2D and 3D seismic surveys. In Figure 2c, we show the borehole logs  
150 drilled in proximity to the 2D and 3D seismic surveys acquired in the study area between 2022 and 2023 (see Figures  
151 1c and 2b for borehole location). The logs include the lithological variation within the top 300 m of the study area and  
152 are later used to constrain the conducted SW analysis interpretation. The borehole logs illustrate that, south of the  
153 mine, the  $2230 \pm 13$  Ma (Burger and Coertze, 1973) Hekpoort Formation basalts constitute the uppermost rocks and  
154 are underlain by the  $2324 \pm 17$  Ma (Dorland, 2004) metasedimentary rocks of the Timeball Hill Formation (Fig. 2c).  
155 Tectonically, the Transvaal Supergroup is structurally complex and has undergone several episodes of deformation  
156 (Veevers, 1981; Vermaak et al., 1994; Coward et al., 1995; Manzi et al., 2013a,b; Nwaila et al., 2022). In particular,  
157 the rocks of the Pretoria Group are displaced by post-Pretoria Group extensional and thrust faults that displace both  
158 the Pretoria Group rocks and the base of the Transvaal Supergroup (Cousins, 1962). The post-Pretoria Group tectonic  
159 events likely led to the reactivation of pre-Transvaal Supergroup faults, which are imaged in the 2003 legacy 3D  
160 seismic data and confirmed by underground drilling and mapping (Manzi et al., 2013a,b; Nwaila et al., 2020a).  
161 Movement along faults inevitably resulted in the creation of numerous fracture systems, which can be observed  
162 underground (if exposed). The study area is also characterised by numerous sills and dykes that intruded at different  
163 geological ages and have been subjected to several investigations. The sills and dykes are of various ages, such as  
164 known post-Karoo dykes of pre-Cretaceous and Cretaceous age (145 - 66 Ma), Karoo (150 Ma), Pilanesberg (1.30  
165 Ga), Vredefort meteorite impact event (2.05 Ga), the Bushveld Igneous Complex magmatism (2.03 Ga), Transvaal  
166 (2.20 Ga), and Ventersdorp (2.60 Ga) (Frimmel, 2014; Frimmel and Nwaila, 2020). Current mining activities can also  
167 reactivate faults and dykes, causing large seismic events, and promoting water infiltration, movement, and circulation  
168 (Masethe et al., 2023). The intersection of water conduits during mining often negatively affects the productivity of

169 the mine and increases the safety risk to mine personnel and infrastructure. Thus, their delineation is important in  
 170 ensuring mine safety, longevity, and increased productivity.



171  
 172 **Figure 2: a) Satellite map showing the legacy 2003 3D Kloof-South Deep and the 2022-2023 3D South Deep Gold Mine**  
 173 **seismic surveys. (b) Zoomed in satellite map of the 2023 South Deep seismic survey. Both satellite maps are plotted using**  
 174 **the WGS 1984 UTM Zone 35S coordinate system. (c) Representative borehole logs located within the study area and**  
 175 **showing the dominant rock types of the top 300 m.**

176

### 177 3 Methodology

#### 178 3.1 Seismic data acquisition

179 Active-source surface 2D and 3D seismic data were acquired between 2022 and 2023 within the framework of the  
 180 ERA-MIN3 Future Project, aimed at imaging the subsurface geology and the orebody at South Deep Gold Mine. The  
 181 acquired two 2D high-resolution seismic lines (P1 and P2, Figs. 1c and 2a, b) were positioned such that they traversed  
 182 the surface zone directly above the mine tunnels, located at a depth of ~ 3.5 km. The 3D seismic survey covers a wider  
 183 area of approximately 4.4 km by 4.7 km, with the mine tunnels located at the centre of the survey area. The acquisition

184 parameters are summarized in Table 1. The 2D profiles were acquired using a 6-ton seismic vibrator (mini-vibe)  
 185 employing a linear sweep of 24 s and a sweep frequency ranging from 2-200 Hz. P1 is north-south orientated and has  
 186 a profile length of 2420 m, while P2 is east-west orientated and has a profile length of 2650 m. The two profiles were  
 187 acquired using 243 and 266 wireless remote acquisition units spaced 10 m apart and connected to 5 Hz vertical  
 188 component geophones, respectively. Two sweeps were generated at every receiver and every second receiver location  
 189 for P1 and P2, respectively.

190 The 3D seismic survey was acquired using two broadband mini-vibes employing a slip-sweep acquisition technique  
 191 with a slip time of 30 s, a single linear sweep of 48 s, and a frequency ranging from 4 to 150 Hz. The grid consisted  
 192 of 9 receiver lines (north-south orientated and 400 m apart), with a receiver spacing of 25 m, and 21 source lines (east-  
 193 west orientated and 225 m apart), and with a source spacing increment of 12.5 m, forming an orthogonal acquisition  
 194 patch. The data were recorded using a total of 1605 wireless remote acquisition units connected to 5 Hz vertical  
 195 component geophones and consisted of 3725 shot points.

196 The units used to record both the 2D and 3D surveys were programmed to switch on at 8:00 am and off at 17:00 pm,  
 197 South African time, during which the seismic data were recorded in continuous mode, at a 2 ms sampling rate. After  
 198 the completion of the survey acquisition stage, all the separate sweeps were later isolated and 6 s of the records were  
 199 extracted from the recording units using the GPS time tagged for each sweep. The layouts of the surveys, however,  
 200 were distorted by natural (river and swamps) and man-made features (mining infrastructure, two large tailings dams,  
 201 roads, and nearby settlements) present in the vicinity of the mine, thus, sharp turns and gaps were introduced in the  
 202 data (crooked profiles; Figs. 1c and 2b). The study area is characterized by a significant but gentle E-W elevation  
 203 variation of approximately 100 m in the southern portion, a gentle 10 m E-W elevation variation in the northern  
 204 section, and a 20 m N-S elevation variation in the middle section of the study area. Throughout the study area, the  
 205 bedrock is largely covered by residual soil. The 2023 South Deep Gold Mine seismic survey was designed to overlap  
 206 with the 2003 Kloof-South Deep survey, which was designed to image the deep-seated Ventersdorp Contact (VCR)  
 207 orebody and major geological structures to assist with mine planning and development (Fig. 2a, Manzi et al., 2012a).  
 208 The acquisition parameters and processing sequence of the 2003 3D seismic survey are summarized by Manzi et al.,  
 209 (2012a,b). In summary, the survey was acquired using 4 vibroseis trucks (sweep: linear, 16s, 12-96 Hz) over an area  
 210 of approximately 96 km<sup>2</sup> with the receiver spacing of 50 m, receiver line spacing of 400 m, shot spacing of 50 m, and  
 211 shot line spacing of 450 m.

212 **Table 1:** Acquisition parameters of the 2D and 3D surveys conducted at South Deep Gold Mine in 2022-23.

<b>Survey Parameters</b>	<b>Profile 1 (P1)</b>	<b>Profile 2 (P2)</b>	<b>3D Survey</b>
<b>Profile length</b>	2420 m	2650 m	4.5 x 4.7 km
<b>Profile type</b>	-	-	Slip-sweep, slip time: 30 s
<b>Sampling rate</b>	2 ms	2 ms	2 ms
<b>Sweep length</b>	24 s	24 s	48 s
<b>Sweep frequencies</b>	2-200 Hz (linear sweep)	2-200 Hz (linear sweep)	4-150 Hz (custom sweep)

<b>Receiver direction</b>	N-S	E-W	E-W
<b>Shot direction</b>	N-S	E-W	N-S
<b>Shot spacing</b>	10 m	20 m	12.5 m
<b>Receiver spacing</b>	10 m	10 m	25
<b>Shot stack</b>	2	2	-
<b>Receiver line spacing</b>	-	-	400 m
<b>Shot line spacing</b>	-	-	225 m
<b>Geophone</b>	5 Hz vertical component	5 Hz vertical component	5 Hz vertical component
<b>Source type</b>	Mini-vibe (6-ton)	Mini-vibe (6-ton)	Mini-vibe (6-ton)
<b>Geodetic survey instrument</b>	Differential Global Positions System (DGPS)	Differential Global Positions System (DGPS)	Differential Global Positions System (DGPS)

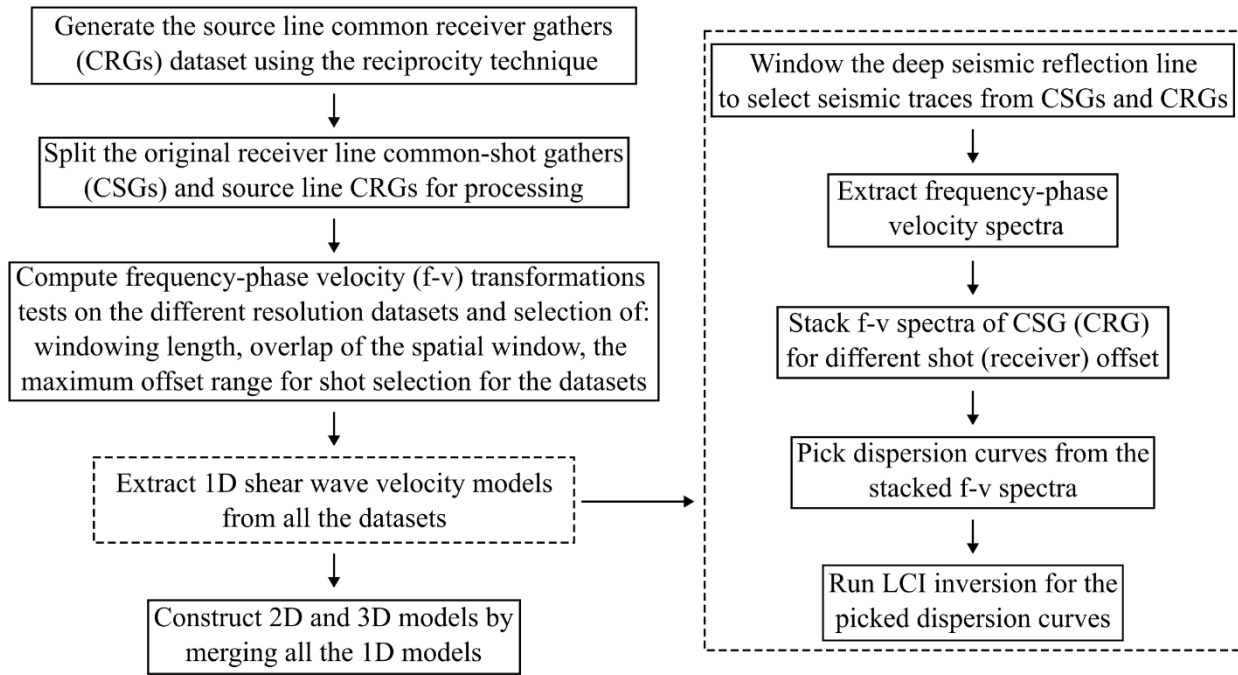
213

### 214 3.2 Data processing

215 The data were subdivided into three datasets: the two 2D lines (P1 and P2); nine E-W oriented receiver lines (R1-R9)  
 216 from the 3D grid; and twenty-one S-N oriented source (shot) lines (S1-S21) from the 3D grid (Fig. 2b). The source  
 217 line dataset was generated from the receiver line dataset by using the reciprocity principle to generate common receiver  
 218 gathers (CRGs) along the source lines. The reciprocity principle states that a wavefield measured at point A generated  
 219 by a point source located at point B is equal to the wavefield measured at point B generated by a point source located  
 220 at point A (Knopoff and Gangi, 1959; Claerbout and Green, 2008; Katou et al., 2017). In seismic investigations, it  
 221 illustrates that the same seismogram will be recorded if seismic source and receiver locations are interchanged,  
 222 irrespective of the geometrical subsurface complexity, as long as the geometry of obstacles and other bodies in the  
 223 vicinity of the source and receiver are fixed (Claerbout and Green, 2008). The implementation of the reciprocity  
 224 theorem was achieved by selecting receivers situated along and near source lines and using them to generate CRGs  
 225 by projecting waveforms recorded at the receivers to their respective shot locations.

226 The MASW technique was applied to the three seismic datasets described above using a workflow based on the  
 227 method by Socco et al. (2009), where a moving spatial window is used along the seismic lines to retrieve a set of local  
 228 SW dispersion curves (DCs). Figure 3 gives a schematic summary of the entire processing workflow. Generally, the  
 229 raw data undergo a data preconditioning that consists of splitting the profiles characterized by severe sharp turns into  
 230 separate segments close to straight lines, as severe profile crookedness distorts the phase shift variation between  
 231 neighboring traces and results in spurious velocities (Lin et al., 2017). The optimal MASW processing parameters,  
 232 i.e., spatial window length, overlap of the moving spatial window, and the maximum offset range for shot selection,  
 233 were defined to obtain a good compromise between spectral and spatial resolution, and the optimal signal-to-noise  
 234 ratio for the dispersion curve analysis by doing some tests (Socco et al., 2009). The spatial window needs to be long  
 235 enough to ensure the recording of longer wavelengths of interest (i.e., the target depth) and small enough not to violate  
 236 the homogeneous media assumption assumed underneath the receiver spread. Meanwhile, the minimum and maximum  
 237 offset ranges are chosen such that they minimize near-and far-field effects and improve the signal-to-noise ratio. For  
 238 each window position, the spectra resulting from different shots falling within the selected offset ranges were

239 computed using the phase shift method (Park et al., 1998) and stacked to improve the signal-to-noise ratio of the  
 240 dispersion image (Grandjean and Bitri, 2006; Neduczka, 2007). From the stacked spectra, the maximum spectral  
 241 amplitude at each frequency, deemed to correspond with the energy of the SW fundamental mode, was automatically  
 242 searched to obtain the local DCs. The DCs were picked through an automatic maxima search and manual cleaning to  
 243 ensure high-quality DC picks. The positions of the DCs were assigned as the center of the windows for which the  
 244 dispersion spectrum was computed.



245

246

**Figure 3: Schematic summary of the entire processing procedure.**

247

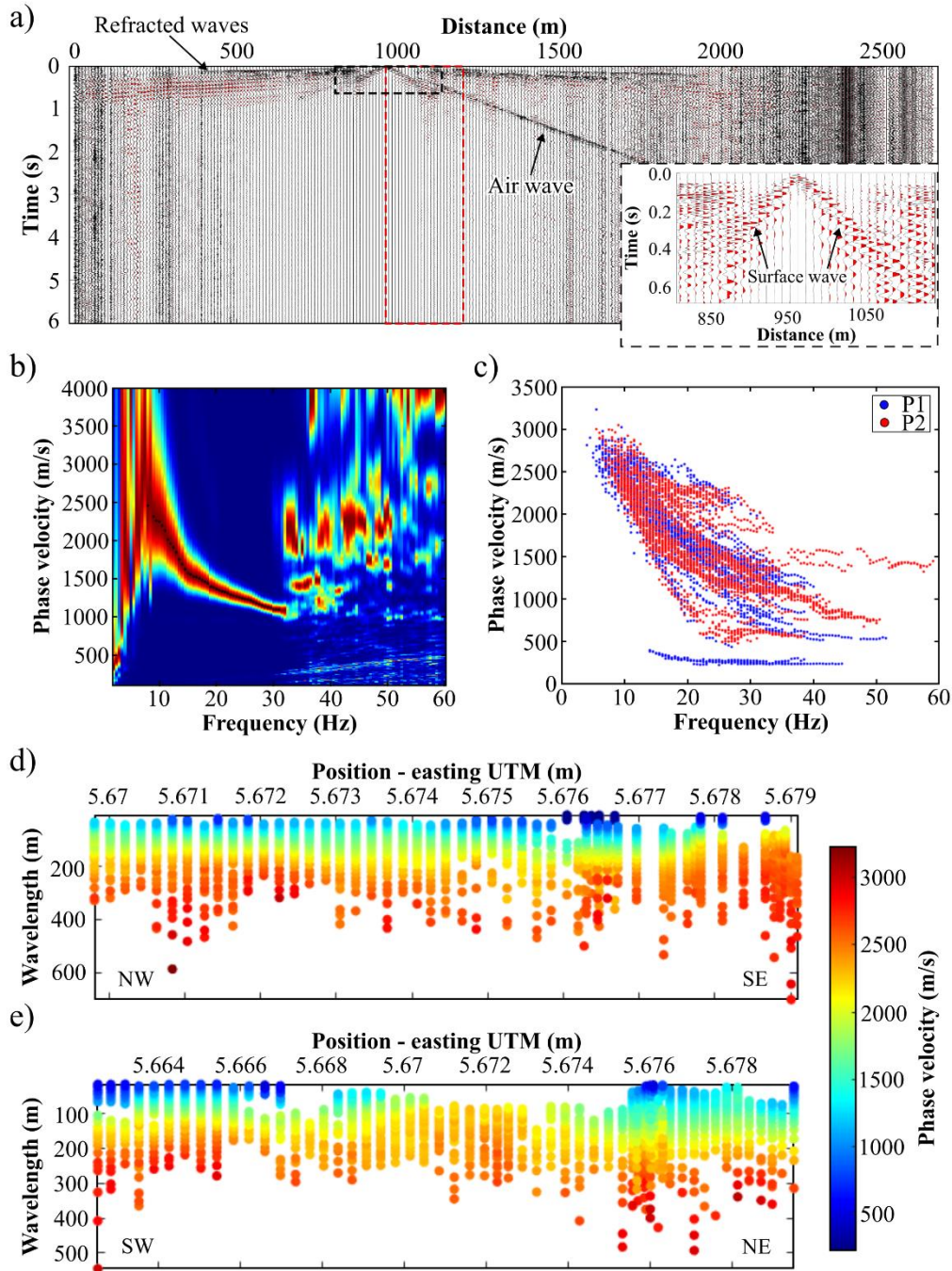
248 In our case, the three datasets have different spatial sampling characteristics that lead to different processing parameter  
 249 choices (Table 2). Due to the receiver spacing, which is 25 m for receiver lines, 12.5 m for shot lines, and 10 m for  
 250 the 2D lines, the spatial windows used to process the data sets are large with respect to usual near-surface SW surveys.  
 251 Typically, for near-surface investigations, data that are acquired on purpose for SW analysis would use receiver  
 252 spacing of 2-5 m. In this case, we use the 3D seismic data acquired for deep exploration and the survey design is not  
 253 optimized for SW. This imposes the use of processing windows larger than those generally used in traditional SW  
 254 surveys, which could result in more local anomalies being suppressed. The spatial sampling is also critical, since a  
 255 large spatial sampling can generate aliasing. In the present dataset, given the higher velocities and the limit on high-  
 256 frequency content, we do not extract wavelengths smaller than the spatial sampling. Moreover, surface wave DCs can  
 257 be extracted at wavenumbers beyond the Nyquist wavenumber (See Socco and Strobba, 2009 for details), hence we  
 258 do not consider spatial aliasing a critical aspect for the processing. The 2D lines (P1 and P2) are those with the denser  
 259 spatial sampling (10 m receiver spacing) and shot layout (10-20 m shot spacing). The utilization of a dense spatial

260 sampling and shot layout allowed the attainment of high signal-to-noise spectra and broad band DCs on 250 m  
 261 windows and a 200 m max offset range. While for the larger 2023 3D seismic survey profiles (i.e., receiver lines R1-  
 262 R9) the shortest window size that provided good quality DCs was 500 m. The shift of the moving window position  
 263 was set equal to the receiver spacing and this led to different densities of DCs along the lines for the three datasets.  
 264 For the two datasets extracted from the 3D grid, the most critical aspect was related to the small number of available  
 265 sources in line with the receivers (or the opposite for the Common Receiver Gathers (CRGs)). The shot spacing along  
 266 receiver lines is 225 m (distance between shot lines), while for the CRGs the “shot” spacing is 400 m (distance between  
 267 receiver lines) leading to very limited stacking of the spectra.

268 **Table 2:** Windowing parameters used for the optimal dispersion curve extraction.

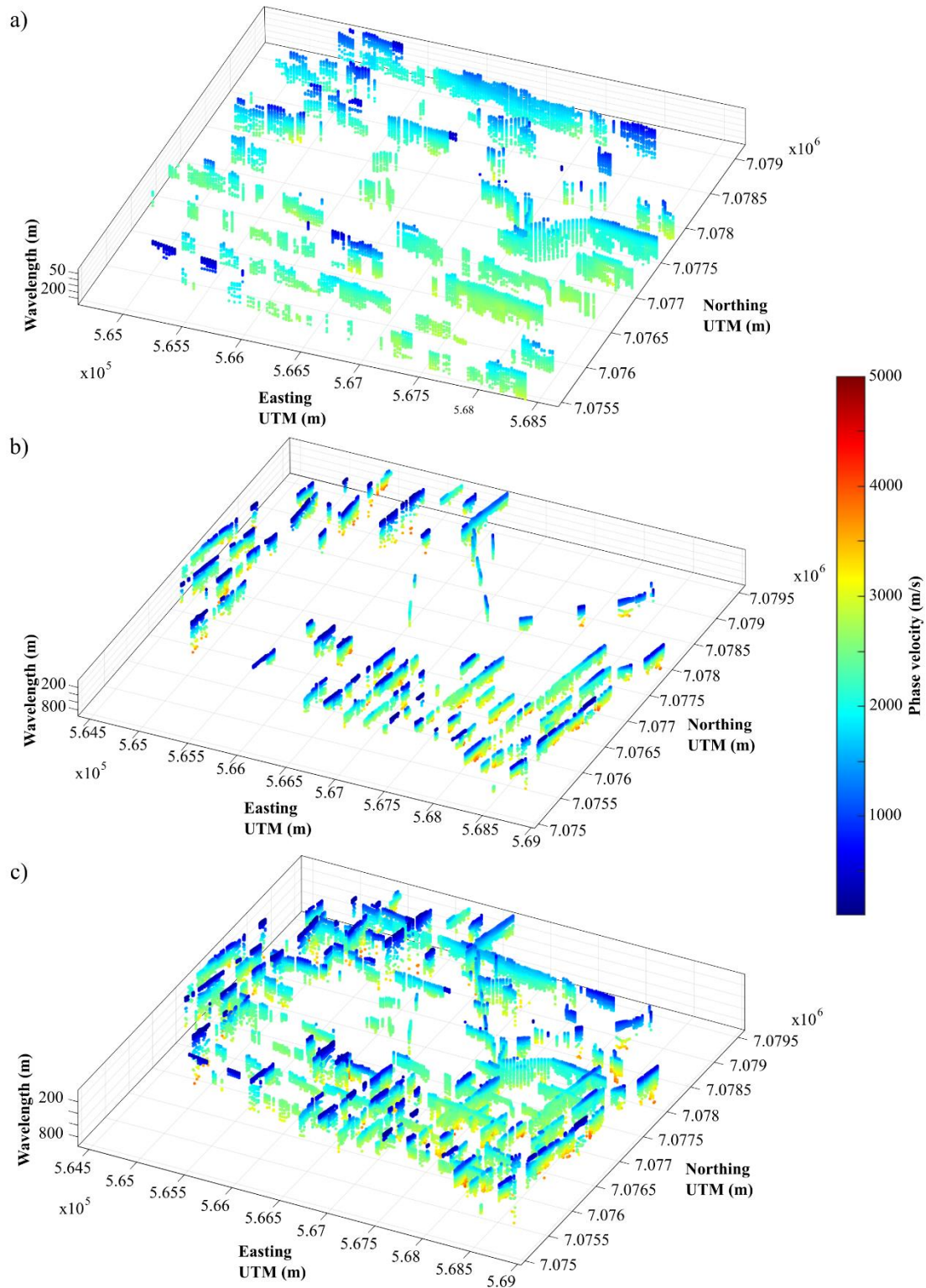
<b>Processing parameters</b>	<b>2D Line</b>	<b>Normal 3D grid receiver lines</b>	<b>Reciprocity lines (source lines)</b>
<b>Minimum window size</b>	250 m	500 m	125 m
<b>Maximum window size</b>	250 m	500 m	250 m
<b>Window stride</b>	10 m	25 m	12.5 m
<b>Minimum offset</b>	10 m	10 m	10 m
<b>Maximum offset</b>	200 m	400 m	400 m

269  
 270 Figure 4a shows an example of a shot gather obtained in the study area, along profile P2. The seismic record in Figure  
 271 4a contains a broad band ground roll that is visible at near-offset traces. Figure 4b gives the frequency-phase velocity  
 272 spectrum obtained after transforming within the red dashed rectangle. The spectrum was obtained after stacking  
 273 spectra from 5 different shots within the set offset range, where the DC (fundamental mode) is picked as the spectral  
 274 maxima. Figure 4c shows all the picked DCs for P1 and P2, while Figure 4d and 4e display them as a function of  
 275 wavelength at their spatial location along the lines. In Figure 4d and 4e, it is remarkable that long wavelengths, i.e.,  
 276 high investigation depths, are achieved thanks to the high velocities prevalent at the site. Figure 5a, 5b, and 5c show  
 277 the DCs that were picked along the 3D grid receiver lines, source lines, and receiver and source lines combined,  
 278 respectively.



279

280 Figure 4: (a) Shot gather from the seismic profile P2, showing the window position (red dashed rectangle) that is later  
 281 transformed into the frequency-phase velocity domain. A zoomed in window showing the surface wave trend visible in the  
 282 record is shown, and its location is indicated using a dashed black rectangle. (b) Frequency-phase velocity spectrum from  
 283 P2 obtained after transforming the highlighted data in Figure (a), where the black dots depict the picked dispersion curve.  
 284 (c) Picked surface wave dispersion curves for profiles P1 (dark blue) and P2 (red), plotted as a function of frequency and  
 285 phase-velocity. In (d) and (e), surface wave dispersion curves for profiles P1 and P2 are plotted as a function of wavelength  
 286 depth and spatial location.

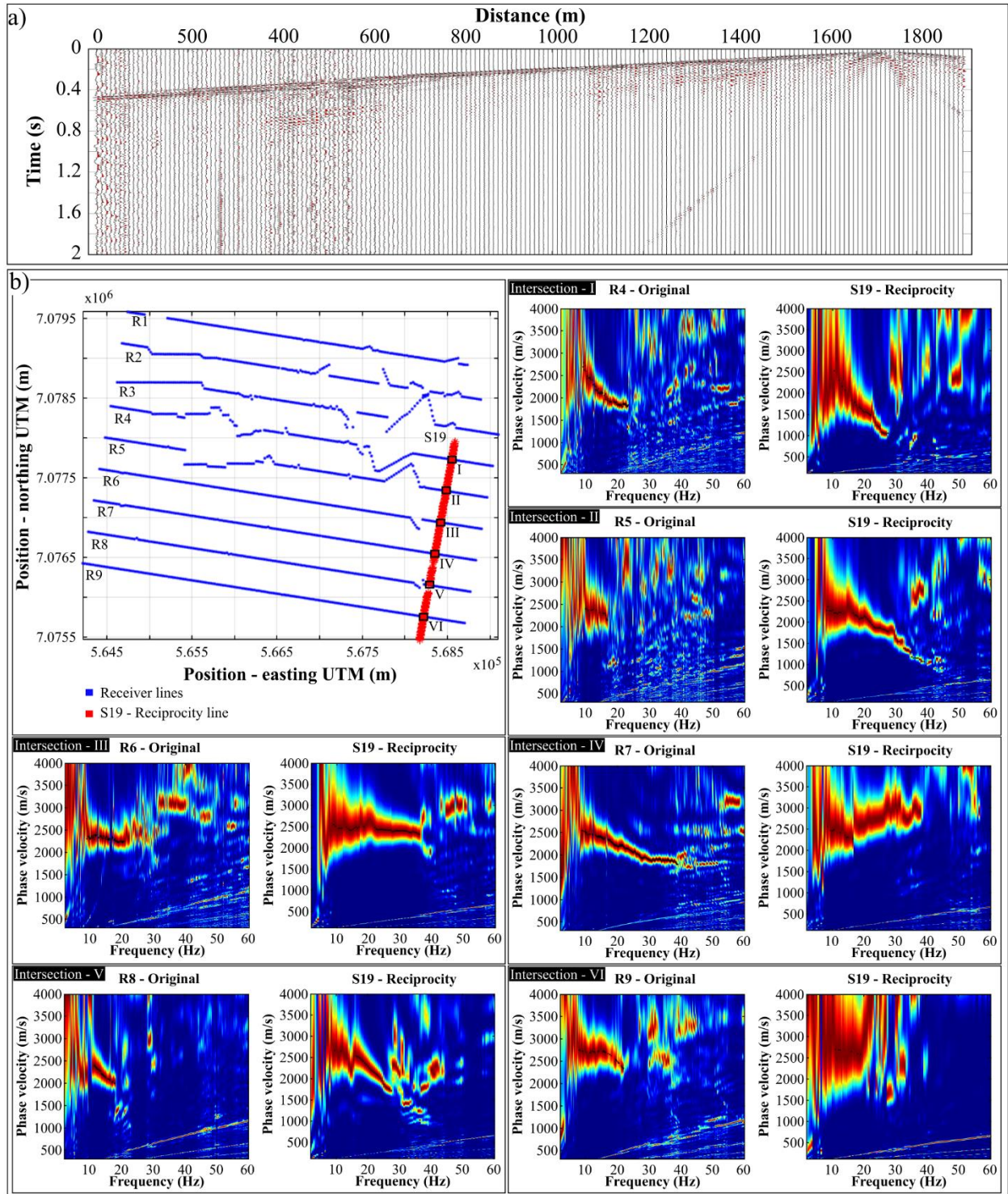


287

288 **Figure 5: Dispersion curves picked along the (a) receiver and (b) source lines. (c) Combined receiver and source line**  
 289 **dispersion curves. The dispersion curves are plotted as a function of wavelength and spatial location.**

290 A total number of 2557 DCs were picked along the 3D grid; 767 of the DCs were extracted along receiver lines, while  
291 1790 (more than twice) were extracted along source lines. The application of the reciprocity principle enabled the DC  
292 density to be increased by  $\sim 230\%$  rounding-off. In the retrieved DC datasets, gaps are present in areas: (1) where the  
293 stacked spectra did not show a clear fundamental mode, thus no DC could be picked, which is possibly due to the  
294 presence of sharp lateral variations within the subsurface, (2) where data could not be acquired due to the presence of  
295 mining infrastructure (e.g., tailings dams, solar panels, satellites, roads, etc.), and (3) where source and receiver lines  
296 are distorted by mining infrastructure.

297 Figure 6a gives an example of a CRG obtained for line S19. To validate the dispersion curves obtained from the CRG  
298 processing, we compared the spectra located at the crossing point for source and receiver lines (Fig. 6b). The  
299 comparison needs to be evaluated taking into consideration that the spectra are computed along two orthogonal  
300 directions and therefore the considered wavefields sample different portions of the subsurface that, given the large  
301 window length, can lead to different phase velocities. We therefore do not expect the spectra to be necessarily equal.  
302 In general, there is a relatively good agreement between the spectra of the two orthogonal lines and spectra computed  
303 from CRGs are broader band than those computed along receiver lines. This is attributed to the traces in CRGs having  
304 a smaller spacing (Table 1). Meanwhile, the spectra from the receiver lines have greater spectral resolution due to the  
305 spectra along these lines being computed using larger spatial windows.

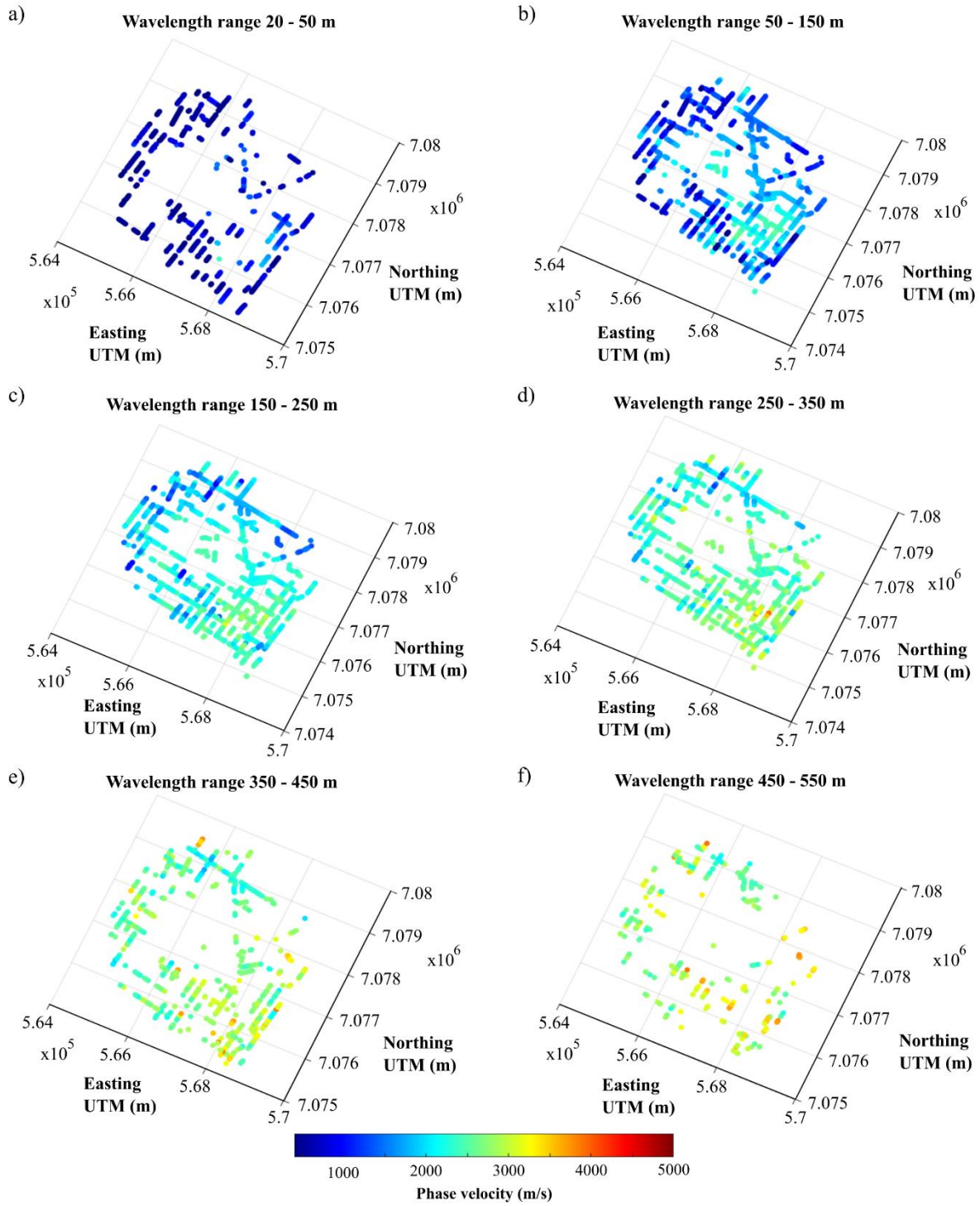


306

307 Figure 6: (a) Example of a common receiver gather obtained along source line S19. (b) Receiver and source line f-v spectra  
 308 obtained at intersection locations I-VI.

309

310 In Figure 7a-f, we show the wavelength coverage of the estimated DCs for the 3D grid as pseudo-slices within different  
311 wavelength ranges, i.e. for progressively higher investigation depths. The highest coverage is achieved for  
312 wavelengths between 50 m and 350 m, but it is still significant up to 550 m over wide areas of the grid.



313

314 Figure 7: Pseudo-slices of the estimated dispersion curves from the site shown using wavelength ranges of (a) 20 - 50 m, (b)  
 315 50 - 150 m, (c) 150 - 250 m, (d) 250 - 350 m, (e) 350 - 450 m, and (f) 450 - 550 m.

316

### 317 3.3 Laterally constrained inversion (LCI)

318 To invert the picked DCs for S-wave velocities, we adopted the LCI scheme. The LCI was first proposed by Auken  
319 and Christiansen (2004) for inverting resistivity data using a pseudo-2D layered parameterization. The LCI is a  
320 deterministic inversion technique that is predicated on an algorithm created for a 1D scheme that makes use of lateral  
321 constraints. A lateral constraint is a parameter that defines the variance permitted for parameters of neighbouring  
322 models (Wisén and Christiansen, 2005; Socco et al., 2009). The constraints represent a spatial regularization that  
323 avoids overfitting the final model. The smaller the expected variance in the area, the stronger the lateral constraints  
324 (Wisén and Christiansen, 2005; Socco et al., 2009). The optimization of the lateral constraints can be done by running  
325 a set of inversions starting from unconstrained and rising gradually the level of constraints until the fitting between  
326 model and data starts to decrease (Boiero and Socco, 2010). The inputs are the DCs and the initial model at the  
327 locations of the DCs. The initial model parameters of the LCI inversion scheme are the layer thicknesses, Poisson's  
328 ratio, density, and S-wave velocities. The technique simultaneously inverts all the picked DCs by minimizing a  
329 common objective function, which incorporates the fitting of data with the model, a priori information, and constraints.  
330 The LCI uses a damped least-squares inversion scheme to update the model iteratively. The initial S-wave velocities  
331 and layer thickness are updated after each iteration, while layer densities and Poisson's ratio are kept fixed (Khosro  
332 Anjom et al., 2024). The final result of the LCI is a S-wave pseudo-2D/3D velocity model.

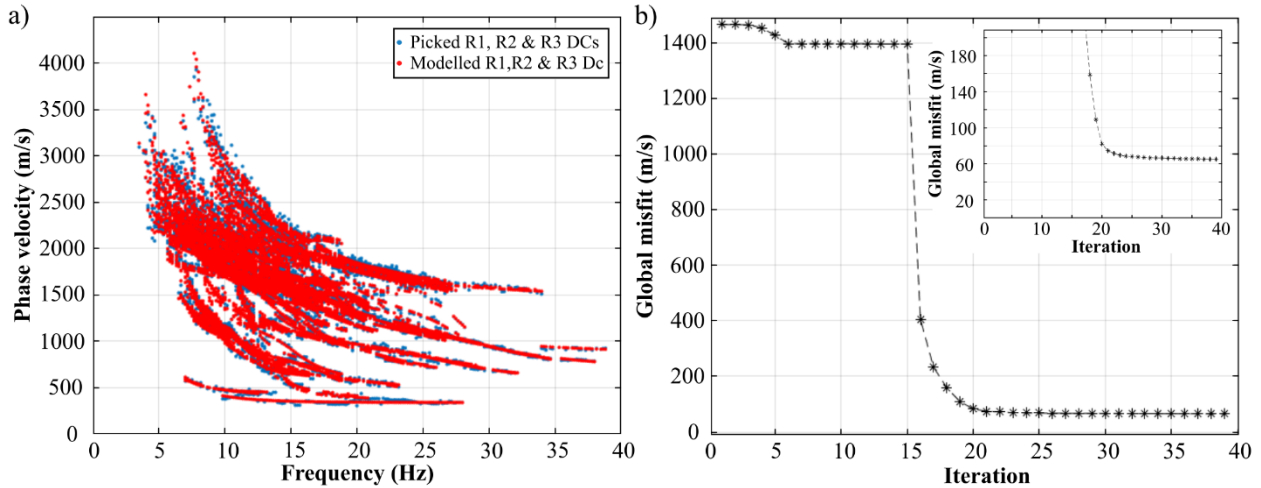
333 In this study, the parameterization of the initial model is laterally invariant, Table 3, and is based on the obtained SW  
334 information and expected geological properties of the site: The initial S-wave velocity model was created from the  
335 picked DCs, while Poisson's ratio and density measurements were estimated based on the materials expected in the  
336 study area (i.e., mainly the partially metamorphosed sedimentary rocks of the Timeball Hill Formation). The maximum  
337 depth of the initial model was set on the basis of a sensitivity analysis with Montecarlo inversion and a wavelength-  
338 depth analysis (Socco et al., 2017) carried out on some sample curves (not shown here). The analysis computed the  
339 relationship between wavelength and investigation depth of the selected DC and showed that DCs with large  
340 wavelengths (Fig. 8e and 8f) have a large investigation depth that goes beyond 300 m. After some inversion tests, we  
341 used a lateral constraint of 700 m/s, which was the maximum level of constraint that could invert the data without  
342 overfitting the picked DCs (Fig. 8a). Figure 8 illustrates an example of the fitting obtained between picked and  
343 modelled DCs for lines R1, R2, and R3 (Fig. 8a), along with the global misfit calculated between the computed and  
344 experimental DCs for each iteration (Fig. 8b). The lowest global misfit obtained after 39 iterations is 65 m/s.

345 **Table 3:** Initial model parameters used to invert the picked dispersion curves.

Layers	S-wave velocity (m/s)	Density ( $g/cm^3$ )	Poisson's ratio	Thickness (m)
1	1000	1.8	0.3	20
2	1020	1.8	0.3	30
3	1200	1.8	0.3	30
4	1500	1.8	0.3	30
5	1500	1.8	0.3	30
6	1700	1.8	0.3	30

7	2000	1.8	0.3	30
8	2500	1.8	0.3	50
9	3000	1.8	0.3	100

346



347

348 **Figure 8: (a) Fitting between picked and modelled (from last iteration) R1, R2, and R3 dispersion curves. (b) Global misfit**  
 349 **between the picked and modelled dispersion curves in (a). The inset in (b) shows a zoomed section of the global misfit.**

350

#### 351 **4 Results and interpretation**

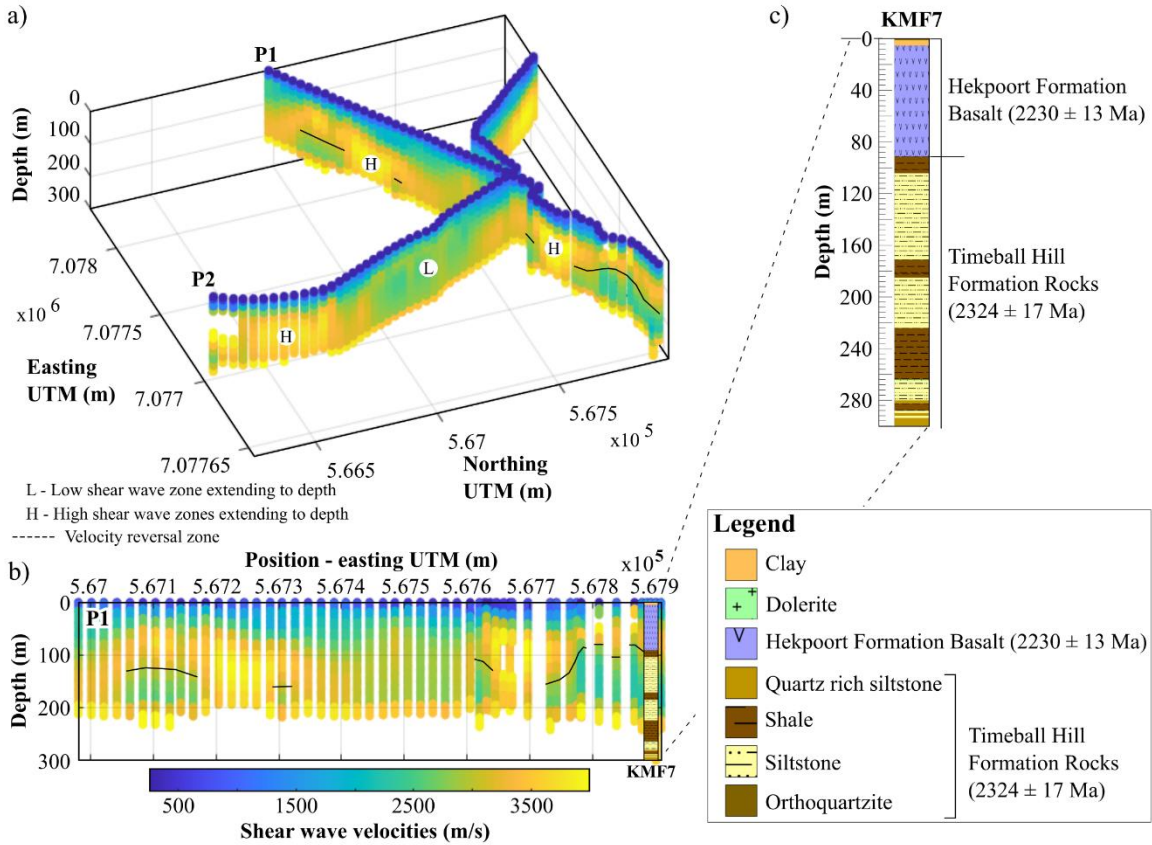
352 Figures 9 and 10 show the near-surface S-wave velocity models obtained through the LCI of the picked DCs along  
 353 the 2D lines (P1 and P2) and 3D grid, i.e., along the receiver and source lines, respectively. In Figures 9, 10, and 11,  
 354 both vertical and lateral velocity geological variations in the study area are resolved.

355 The results of the inversion showed significant update with respect to the initial model, as confirmation of the  
 356 sensitivity of the data to model parameters. Velocity reversal zones with spatial consistency appeared in several zones  
 357 of the final 2D/3D models. Since the initial model does not contain any velocity reversal, we consider them a reliable  
 358 feature in the final models. The spatial consistency of the velocity of the layers is not due to the introduction of the  
 359 lateral constraints since the low velocity zones were present also in the unconstrained inversion we carried out as a  
 360 benchmark to define the optimum level of constraints. As far as the investigation depth is concerned, we tested the  
 361 sensitivity through the wavelength-depth analysis and, in certain zones of the final velocity models, we saw significant  
 362 updates with respect to the initial model, down to a depth greater than 300 m. In other zones, instead, a lower  
 363 penetration depth was reached. We hence plotted the final models using a variable depth, based on the penetration  
 364 depth of the DCs. The estimated velocities are in line with the expected values for the formations. The expected  
 365 vertical resolution is  $\sim 20$  m in the upper part of the model and  $\sim 40$  m in the deeper part of the model, consistent with  
 366 the selected initial model. The lateral resolution is related to the DC density along the line (from 10 to 25 m) but is  
 367 also affected by the smoothing effect of the processing windows (125-500 m) (Table 2).

368

369 **4.1 Lithological layering, faults, and intrusions**

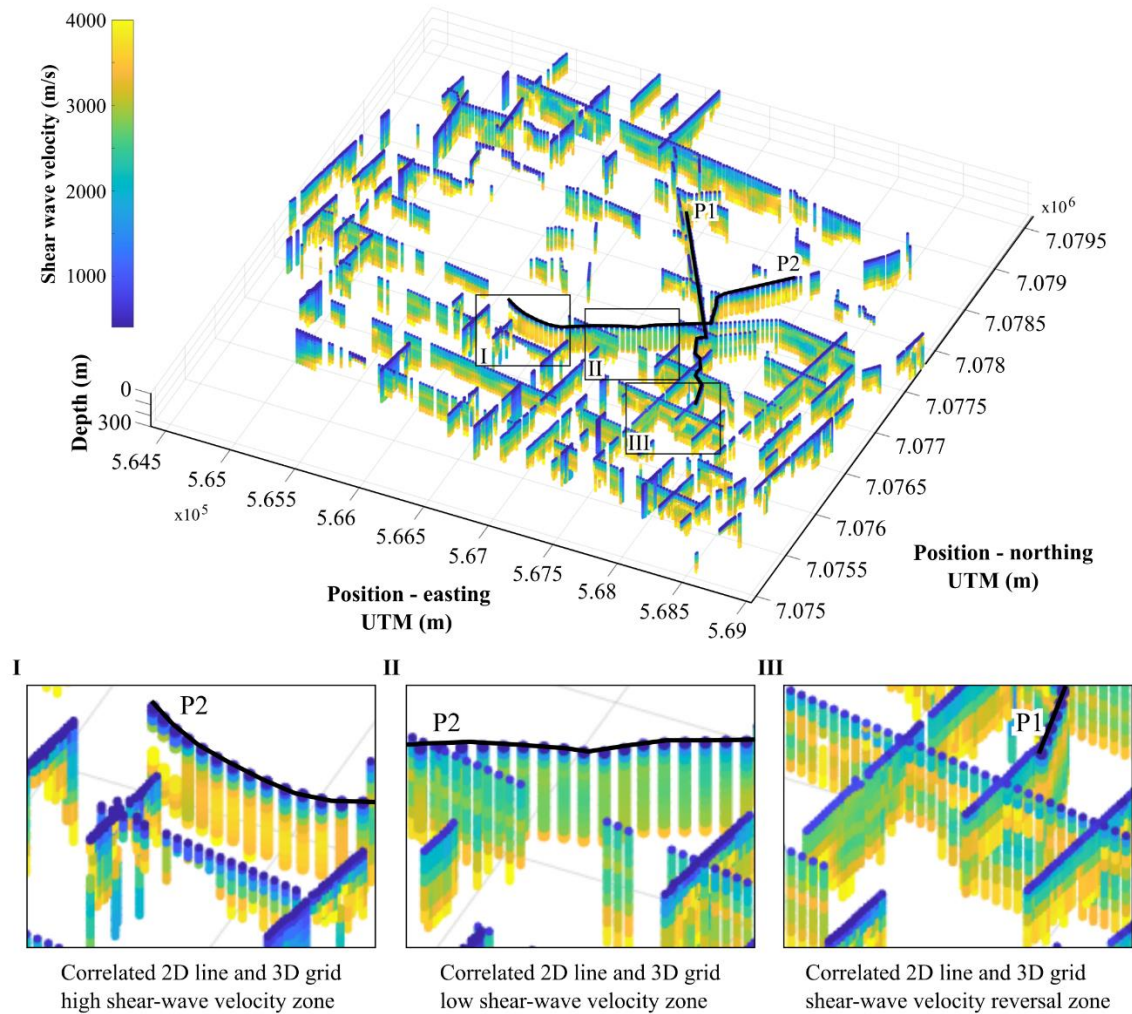
370 From the obtained high-resolution 2D S-wave velocity models, for P1 and P2 (Fig. 9), notable is that the site is  
 371 characterized by a prominent (1) velocity reversal zone (indicated with a black solid line) due to lithological changes  
 372 (Fig. 9b and c) and (2) low- and high-velocity zones that extend from the surface to great depths (i.e., > 150 m).  
 373 Evident in Figure 10 is that the S-wave high (I), low (II), and reversal (III) velocity anomalies are also resolved in the  
 374 3D grid S-wave velocity model. A good anomaly spatial location and velocity correlation is observed between the 2D  
 375 and 3D models within the high-velocity, low-velocity, and velocity reversal zones (Fig. 10). In the 3D S-wave velocity  
 376 model, the velocity reversal zone is overlain by a high-velocity zone with a sheet-like geometry (i.e., near-horizontal  
 377 and planar-orientated, Fig. 10).



378

379 **Figure 9: (a) 3D plot of the high-resolution 2D shear-wave velocity models (i.e., P1 and P2). (b) P1 pseudo-2D S-wave velocity**  
 380 **model shown along with the borehole (i.e., KMF7) located along the line. (c) Zoomed image of the borehole KMF7 showing**  
 381 **the depth scale, formations, and rock types located in the area.**

382



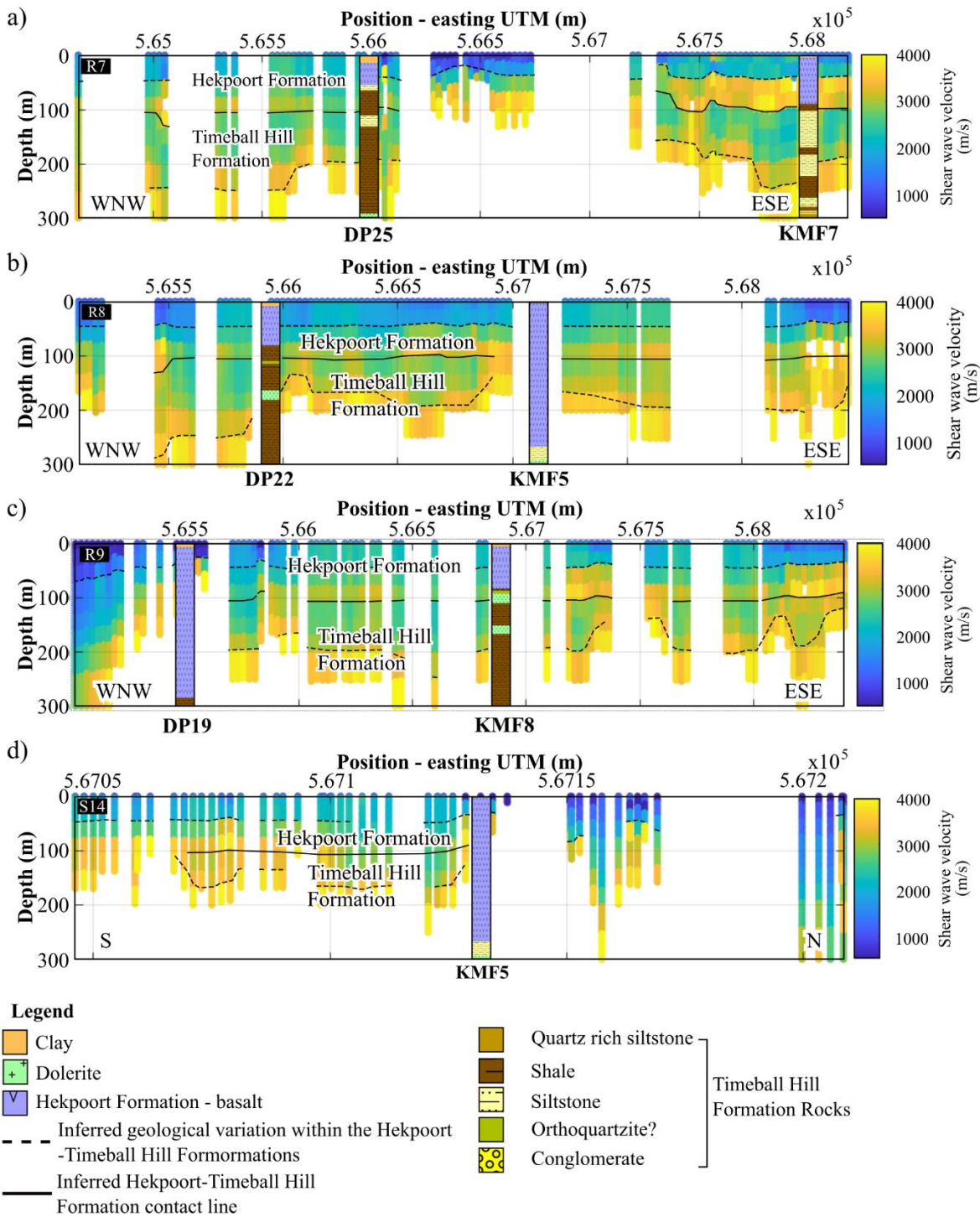
383

384 **Figure 10: South Deep Gold Mine 2D and 3D grid data plot. The rectangles I, II, and II indicate correlating high, low, and**  
 385 **velocity reversal zones between the obtained 2D and 3D S-wave velocity models, respectively.**

386

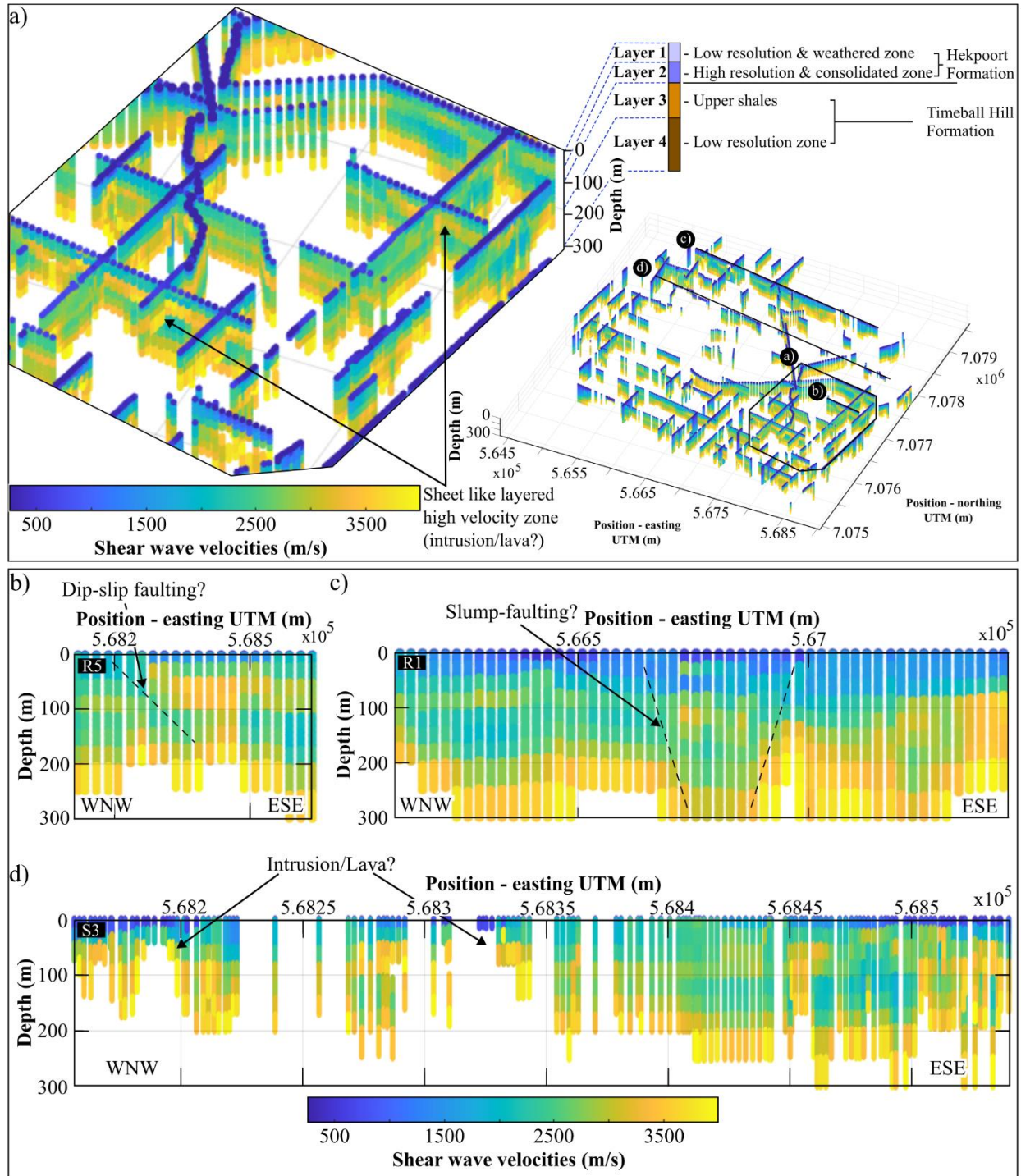
387 Figure 11 illustrates the correlation between available surface borehole logs in the study area and the S-wave velocity  
 388 profiles closest to them. Apparent in Figures 9b, c, and 11a is that the identified velocity reversal zone (indicated by  
 389 a solid black line) marks the boundary/contact between the overlying basalts of the Hekpoort Formation and the  
 390 underlying shales and siltstones of the Timeball Hill Formation. Also notable in Figures 9b, 11a and b is that where  
 391 the depth extent of the uppermost Hekpoort Formation rocks is greater than ~ 50 m and less than ~ 200 m, the contact  
 392 between the Hekpoort Formation and Timeball Hill Formation is mapped relatively well; while in areas where the  
 393 thickness of the Hekpoort Formation is greater than ~ 200 m (Fig. 11b and c), the Hekpoort-Timeball Hill Formation  
 394 contact cannot be resolved. Indicated by the black dashed lines are the significant lateral variations present within the  
 395 rocks of the Hekpoort and Timeball Hill Formations, which are elaborated more in the following section. This

396 comparison of S-wave velocity profiles and proximal borehole information illustrates that the obtained S-wave  
 397 velocities are sensitive to the lithological variation characteristic of the site and are reasonable and reliable.



398  
 399 **Figure 11: Representative boreholes of the study area projected on pseudo-2D S-wave velocity models constituting the 3D**  
 400 **grid that are closest to them. Pseudo-2D S-wave velocity models of lines: (a) R7, (b) R8, (c) R9, and (d) S14.**

401  
402 In general, within the top 300 m of depth, the overall S-wave velocity is interpreted to show four sheet-like subsurface  
403 layers (Fig. 12a). The first layer roughly extends from the surface to a depth of ~ 40 m and has S-wave velocity ranging  
404 from < 500 m/s to ~ 2500 m/s. The second layer shows higher velocities (~ 2500 m/s to ~ 3500 m/s) and extends from  
405 ~ 40 m to 120 m below the surface. A third layer, with S-wave velocities similar to the first one, extends from ~ 120  
406 m to 200 m. The last resolvable layer is a high-velocity zone (> ~3500 m/s), extending from ~ 200 m of depth (Fig.  
407 12a). The first two identified layers belong to the Hekpoort Formation and are interpreted to constitute the weathered  
408 and least weathered zones of the Hekpoort Formation rocks, respectively. The last two layers belong to the upper  
409 shales of the Timeball Hill Formation; the high velocities in the second layer of the Timeball Hill Formation are  
410 attributed to the presence of sills at those depths, see Figure 2c. During the emplacement of ultramafic-mafic rocks of  
411 the Transvaal Supergroup, shale- and quartzite-dominated formations (i.e., Timeball Hill, Boshhoek, and Daspoort  
412 Formations) formed preferential sill emplacement locations as compared to the carbonate and volcanic formations of  
413 the Supergroup. The shales and quartzite formations, being preferential emplacement locations, are linked to the  
414 abundant parting surfaces within shales (i.e., fissility) and the prevalent upper and lower contacts between thick  
415 quartzites with under- and overlying-shales (Button and Cawthorn, 2015). The transition from the basaltic Hekpoort  
416 Formation rocks (high seismic velocity rocks) to the metasedimentary rocks of the Timeball Hill Formation (low  
417 seismic velocity rocks) results in the velocity reversal zone observed between the second and third layers, indicated  
418 by a solid black line in Figures 9 and 11. Considered, however, is that the presence of a velocity reversal results in a  
419 reduction in the reliability of S-wave velocities of layers located below the reversal zone. Velocity reversal zones  
420 reduce the penetration of large wavelengths into the underlying layers since the wavefield energy is trapped into the  
421 low velocity layer, thus reducing the mapping resolution and velocity reliability at depth (Groves et al., 2011).  
422 Additionally, SW analysis suffers from a reduction in resolution with depth and, due to this, not much interpretation  
423 is drawn on the exact S-wave velocities observed within the last layer. The prevalence of the velocity reversal zone  
424 throughout the study area suggests that the Hekpoort Formation is present throughout the vicinity of South Deep Gold  
425 Mine, contrary to what is observed in the local geological map of the area (Fig. 1c). This is supported by the presence  
426 of Hekpoort Formation basalts in areas where Timeball Hill Formation rocks are reported to be outcropping (see  
427 boreholes KMF5, KMF6, and KMF7 in Figure 1c). However, the confirmation of this interpretation is hampered by  
428 the lack of available borehole data around the center and northern area of the mine. The depth, thickness, and S-wave  
429 velocities of the imaged lithologies and corresponding layers are variable, and in some areas, are disturbed by low and  
430 high-velocity zones that extend from the near-surface to depths beyond that resolved by the survey (Fig. 12b-d). These  
431 high- and low-velocity zones are discussed in the following section.



432

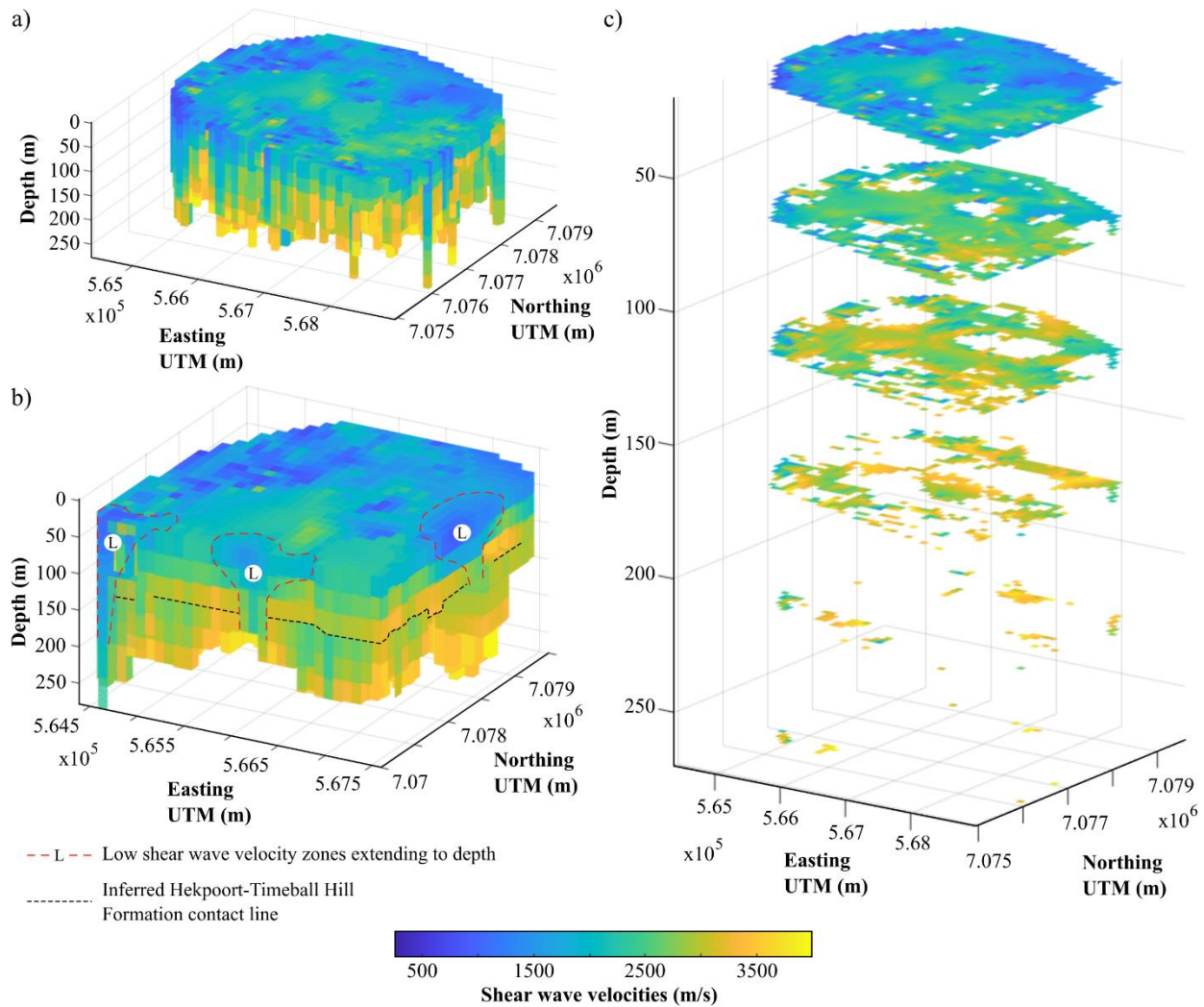
433 Figure 12: Local features observed at the site. (a) Sheet-like layering; (b) dip-slip faulting; (c) slump-faulting; and (d)  
 434 intrusions/lavas. Shown in the 3D grid in (a) are the locations of the zoomed in 3D grid displayed in (a) and the locations of  
 435 the S-wave velocity sections in (b), (c), and (d), respectively.

436

437 The low-velocity zones are interpreted to be associated with dip-slip (Fig. 12b) and slump-faulting (Fig. 12c). The  
438 reduction in S-wave velocities within fault zones is attributed to increased fracturing, porosity, and fluid content,  
439 which lead to the physical breakdown (weathering and alteration) of the primary minerals in the in-situ rock into less  
440 dense secondary phases. This transformation reduces the rock's elastic moduli, ultimately lowering seismic velocities.  
441 According to Mutshafa et al. (2023), weathering of the rocks in the study area is highly variable and can extend to  
442 depths greater than 500 m, which is consistent with the presented findings. The interpreted dip-slip faulting, in Figure  
443 12b, shows relative vertical displacement between the rocks above and below the fault plane. Meanwhile, the slump-  
444 faults, Figure 12c, are largely characterized by wide near-surface footprints that taper down with depth, i.e., they  
445 progressively get narrower with depth. In the slump zone, the layers (including the overlying volcanic rock layers)  
446 are observed to be sunken. The identified faulting and possible intrusions are characteristic of the study area and  
447 consistent with the findings of Cousins (1962) and Parsons and Killick (1990). Cousins (1962) documents that the  
448 rocks of the Pretoria Group are displaced by post-Pretoria Group faults that displace both the Pretoria Group rocks  
449 and the base of the Transvaal Supergroup, and slump-faulting, which only affects the formations within the Transvaal  
450 Supergroup, but not the base of the Transvaal Supergroup. Cousins (1962) interpreted these faults as slump-faulting  
451 originating from the subsidence of the dolomitic units of the Transvaal Supergroup, situated within a formation  
452 underlying the Pretoria Group Formations.

453 High-velocity zones, extending from the near-surface to depth or terminating within the upper subsurface, are observed  
454 in Figures 9a, 10, and 11b–d. In Figure 11b–d, these zones correlate with thick basaltic lava flows of the Hekpoort  
455 Formation. The termination of S-wave velocities at depth reflects the penetration depth and the influence of complex  
456 structural features and abrupt lithological heterogeneities.

457 Figure 13a-c illustrates the interpolated 3D model view of the grid acquired at the mine and depth slices (i.e., velocity  
458 maps) extracted from the 3D model. Figure 13a displays the velocity model of the survey area in 3D. The zones  
459 marked by dashed red lines in the vertically sliced 3D model, Figure 13b, illustrate the coherency and depth extent of  
460 the low-velocity zones in the area and their interaction with the reversal zone (shown using a black dashed line and  
461 situated at a depth of ~ 120 m). The velocity maps in Figure 13c better illustrate the increase of velocities with depth  
462 and the presence of low-velocity zones that extend from the near-surface to greater depths.



463

464 **Figure 13: (a) 3D S-wave velocity model of the study area. (b) Cropped 3D S-wave velocity model showing the velocity**  
 465 **reversal zone (indicated by the black dotted lines) and low velocity zones that extend from the surface to greater depths**  
 466 **(indicated by the red dotted lines). (c) 3D S-wave velocity model depth slices illustrating the general variation of S-wave**  
 467 **velocities with depth.**

468

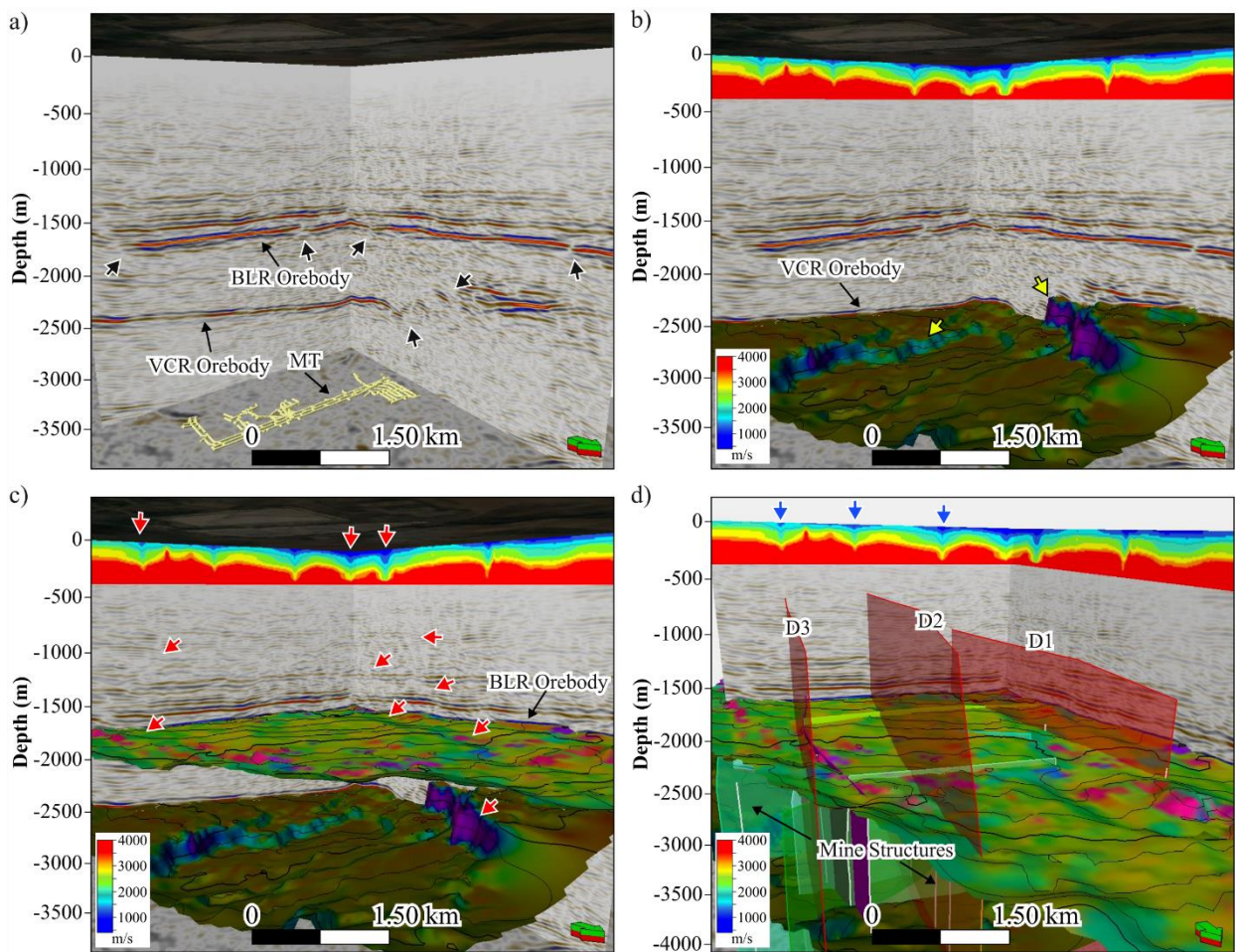
#### 469 **4.2 Structural linkage between shallow aquifers and deep mining levels**

470 To investigate the structural geology linkage between shallow aquifers and deep mining levels, we integrated our  
 471 shallow 3D Vs model with the legacy 2003 3D reflection seismic data acquired for deep gold exploration, mine  
 472 planning, and development (Fig. 14a-d). The legacy 3D seismic survey covers both the South Deep Gold Mine and  
 473 Kloof Gold Mine and was primarily acquired to map the VCR orebody and major fault systems (Manzi et al., 2012a).  
 474 The base of the 2.65–2.05 Ga Neoproterozoic–Paleoproterozoic Supergroup horizon (Black Reef, ~ 0.5 km below ground  
 475 surface) and the mine orebody (VCR, ~ 3 km below ground surface) are well-defined by the legacy 3D seismic data

476 (Fig. 14a-d). Both the VCR orebody and the base of the Transvaal Supergroup (i.e., BLR orebody) are cross-cut by  
477 several faults with variable throws and orientations (indicated by black and red arrows in Fig. 14a). Large-scale faults  
478 mainly cross-cut the VCR orebody and underlying strata (indicated using yellow arrows, Fig. 14b). In contrast, several  
479 small-scale faults and dykes cross-cut the entire stratigraphy (e.g., VCR and BLR orebodies, and the Transvaal  
480 Supergroup rocks) as indicated by red arrows in Fig. 14c. Manzi et al. (2012b) spatially correlated the geological  
481 structures (faults and dykes) defined by the 2003 legacy seismic data at the VCR mining level with groundwater  
482 intersected through underground drilling data. The integrated data showed a good spatial correlation between water  
483 and geological structures. Manzi et al. (2012b) hypothesized that the water found at the mining level originates from  
484 the overlying near-surface fractured aquifer systems of the Transvaal Supergroup and travels through faults and dykes  
485 to the mining levels. However, due to the low resolution of the large-offset 2003 legacy 3D seismic data in the near-  
486 surface, the continuity of these faults and dykes into the overlying aquifer systems was never fully investigated (see  
487 Fig. 14a-b). This study attempts to provide some seismic constraints on the near-surface geology and previous  
488 interpretations using the SW analysis of the 2023 3D seismic data. Figure 14d shows the integration of 2003 depth-  
489 converted pre-stack time migrated seismic data, pseudo-2D S-wave sections extracted from 2023 3D seismic data,  
490 mine infrastructure (e.g., mining tunnel – MT), and mine geological structures (faults and dykes). Smoothing, by  
491 increasing the gridding bin size, was applied to the presented S-wave section to suppress the more local variations  
492 (i.e., subtle variations such as layering) and enhance the visibility of larger (regional) scale trends present in the S-  
493 wave data. As stated already, Figure 14 shows that the P-wave seismic section lacks reflectivity in the near-surface  
494 (top ~ 0.5 km); however, it exhibits strong reflectivity at deeper depths, i.e., between depth intervals of ~ 0.5 km to  
495 3.5 km (Fig. 14a). Overlying the S-wave velocity model on the P-wave section enables near-surface variations and  
496 structural complexity resolved by the S-wave velocity model, to be viewed with respect to deeper structures well  
497 resolved by the P-wave seismic reflection method, including known water-bearing structures at the mining levels (Fig.  
498 14c-d). The mine modelled and confirmed water-bearing geological structures at the mining levels include the three  
499 north-south trending dykes (here referred to as D-1, D-2 and D-3) that cross-cut the gold orebodies (VCR and Upper  
500 Elsburg Reef package) at depths between 3 and 3.5 km below the ground surface (Fig. 14d). The source of the water  
501 found at the mining level, along these dykes, is unknown. Furthermore, the continuity of these structures above the  
502 mining levels is not known since they are not well-defined on the current legacy seismic data. In determining the  
503 linkage of these dykes with the overlying aquifers, we analysed the near-surface S-wave velocity zones and  
504 investigated their spatial correlation with these dykes. The assumption is that, if the targeted structures intersect the  
505 aquifers, then they have the potential to transport water from the overlying Chuniespoort Group dolomite aquifers to  
506 the underground workings (Manzi et al., 2012b).

507 Figure 14d shows near-surface low-velocity zones (indicated by blue arrows, and with velocities varying from ~ 500  
508 m/s to 4000 m/s) that may correspond to known major dykes (D-1, D-2, and D-3) and fault zones present in the vicinity  
509 of the mine and confirmed by underground mapping and drilling. The locations of the low-velocity zones on the S-  
510 wave section correlate well with the locations of the apparent fault zones and dykes imaged at the VCR mining level.  
511 The S-wave low-velocity zones are possibly structurally weak zones (e.g., fault zones) that allowed for dyke  
512 emplacement or are the weathered tops of the dykes. The dykes are mafic in composition and less competent in the

513 near-surface compared to silicate rocks, and therefore break down easily than the surrounding rocks, resulting in lower  
 514 seismic velocities relative to the surrounding rocks (Evans et al., 1998). Noted on the seismic sections is that the  
 515 reflector disturbances associated with these faults and/or dykes are not well-defined within the upper units of the  
 516 Transvaal Supergroup (i.e., above the BLR orebody). This could be because (1), in the case of faults, their throws are  
 517 not large enough to be resolved by the seismic data, and (2), in the case of the dykes, they are near-vertical with a  
 518 thickness less than the resolution limit of the legacy seismic reflection data. These dykes and linked near-surface low-  
 519 velocity zones are possible water source preferential flow-pathways that act as pathways for water migration from the  
 520 Chuniespoort Group dolomites into the VCR and UER mining levels. Several similar dykes and faults that displace  
 521 both the BLR and VCR orebodies in the area were detected through seismic attributes, and are reported by Manzi et  
 522 al. (2012b).



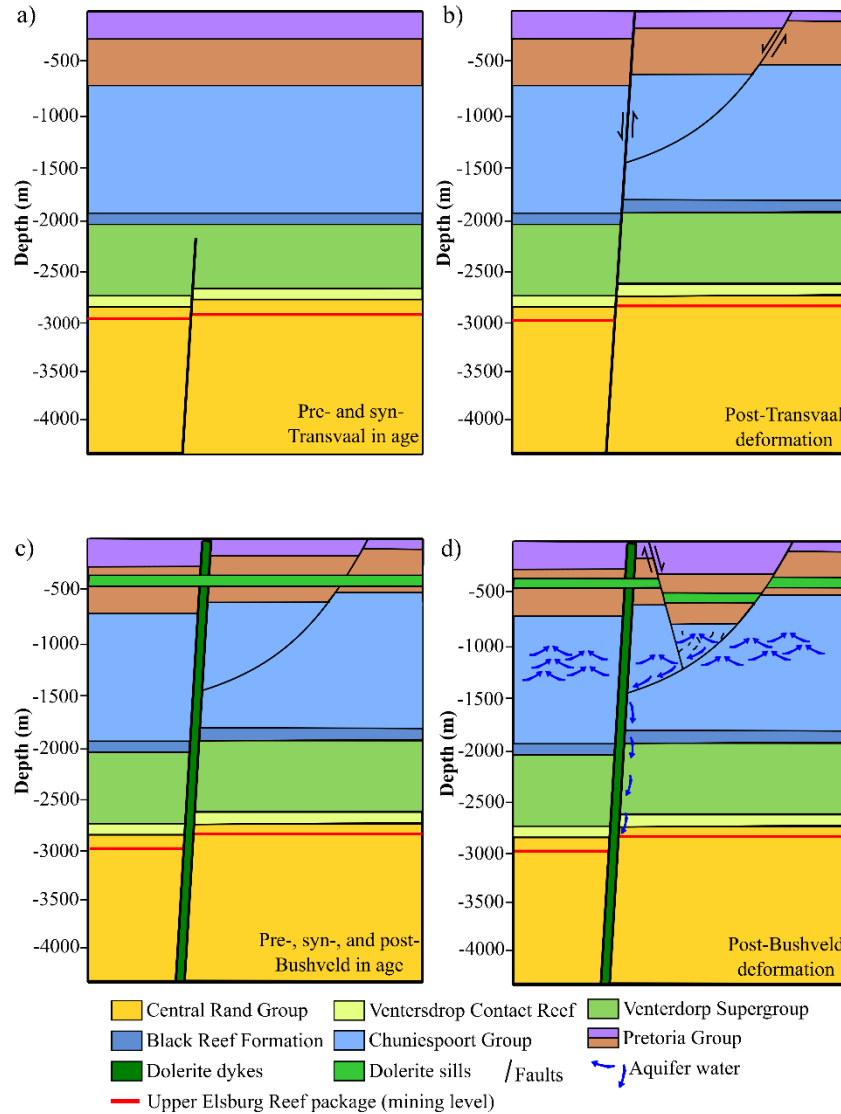
523  
 524 **Figure 14: Integration of the P-wave reflection seismic data and S-wave velocity models.** (a) Pre-stack time migrated seismic  
 525 section (depth converted) extracted from the 2003 legacy 3D South Deep Gold Mine seismic data. The reflection seismic  
 526 data show strong and continuous reflections related to the Black Reef (BLR) unconformity, and Ventersdorp Contact Reef  
 527 (VCR) orebody, and the location of the mining tunnels (MT). The black arrows point to faults that displace the BLR and  
 528 VCR unconformities. (b) P-wave reflection seismic sections with the near-surface S-wave velocity model and VCR dip  
 529 attribute map. The yellow arrows point to large-scale faults displacing the VCR orebody. (c) P-wave reflection sections with  
 530 the BLR dip-azimuth attribute map and VCR dip attribute map. The red arrows point to small-scale faults that seem to  
 531 cross-cut the entire stratigraphy. (d) Integrated 2003 depth-converted pre-stack time migrated seismic data, near-surface

532 S-wave velocity model, and mine geological structures (faults and dykes (D-1, D-2, and D-3)). The blue arrows indicate  
533 surface zones that appear to exhibit potential linkages with the geological structures (faults and dykes) observed at the  
534 mining level and imaged by the legacy 2003 3D reflection seismic data.

## 535 **5 Discussion**

### 536 **5.1 Subsurface conceptual geological model drawn from the integrated datasets**

537 Overall, the S-wave velocity results attained in this study iterate the advantages and advances that can be made from  
538 computing SW analysis on deep reflection seismic profiles. Comparing the geological information interpreted from  
539 the S-wave velocity models with proximal borehole data and known geological characteristics of the area illustrates  
540 that the subsurface information inferred from the S-wave velocity models is in agreement with a priori information.  
541 In Figure 15, we provide a geological model and constrain the tectonic history of a portion of the Witwatersrand basin,  
542 focusing on the deeper pre-Transvaal Supergroup and post-Bushveld tectonic events within the South Deep Gold  
543 Mine. The geological model focuses on the combined near-surface and deeper P-wave reflection seismic, mine  
544 mapping, and drilling information. The geological model commences with the deposition of the Central Rand Group  
545 of the Witwatersrand Supergroup and the subsequent emplacement of the basaltic lavas of the Ventersdorp Supergroup  
546 (Fig. 15a). This is followed by a pre-Transvaal deformation event that displaces the stratigraphy of both the Central  
547 Rand Group and Ventersdorp Supergroup, respectively (Fig. 15a). Subsequently, the Chuniespoort and Pretoria  
548 Groups of the Transvaal Supergroup are deposited (Fig. 15a). A post-Transvaal deformation event occurs thereafter,  
549 reactivating pre-existing faults, forming faults that displace the entire stratigraphic sequence including the Transvaal  
550 Supergroup and consists of associated splay faults (Fig. 15b). The faults act as planes of weaknesses and serve as a  
551 pathway for preferential emplacement of intrusions (doleritic dykes) during pre-, syn-, and post-Bushveld event (Fig.  
552 15c). Doleritic sills are emplaced at an angle to the doleritic dykes along bedding planes of the Pretoria Group rocks  
553 (Fig. 15c). Lastly, slump faulting (post-Bushveld deformation) occurs due to the dissolution of dolomites of the  
554 Chuniespoort Group and displaces the overlying Chuniespoort and Pretoria Group rocks (Fig. 15d).



555

556 **Figure 15: Generalized geological model illustrating the sequence of geological and deformation events identified within the**  
 557 **study area: (a) deposition of the Central Rand Group and subsequent emplacement of the Venterdorp Supergroup,**  
 558 **followed by a pre-Transvaal deformation event, and thereafter, the deposition of the Transvaal Supergroup (Chuniespoort**  
 559 **and Pretoria Groups); (b) faulting associated with a post-Transvaal deformation event occurs reactivating pre-existing**  
 560 **faults and displaces the entire stratigraphic sequence; (c) the intrusion of doleritic dykes and sills along planes of weaknesses**  
 561 **such as faults and bedding planes (pre-, syn-, and post- Bushveld in age); (d) slump-faulting associated with the dissolution**  
 562 **of dolomites results in the displacement of the overlying Chuniespoort and Pretoria Group rocks (post-Bushveld**  
 563 **deformation). The dolomites of the Chuniespoort Group act as water sources (aquifers) and are displaced by faults and**  
 564 **dykes that link them to the Upper Elsberg Reef package (underground workings at depth) and thus, act as pathways for**  
 565 **water migration from the near-surface to underground workings (water preferential flow-pathways).**

566

567 **5.2 Delineating water preferential flow-pathways using shallow and deeper velocity models along with mine**  
568 **mapping and drilling information**

569

570 Gold-bearing strata of the West Rand Goldfield are overlain by an approximately 1 km thick Chuniespoort Group  
571 dolomite sequence, which is associated with karst systems that host considerable volumes of water (Fig. 15d,  
572 Wolmarans, 1984; Van Niekerk and Van der Walt, 2006). The dolomitic aquifers are compartmentalized by several  
573 fracture zones, fault zones, and dykes that link them to the underground workings and act as pathways of water  
574 migration from the near-surface to underground workings (water preferential flow-pathways) (Fig. 15d, Manzi et al.,  
575 2012b). Thus, water inflow in mining districts and water inrush are some of the serious and difficult-to-predict  
576 challenges that affect mining processes and efficiency at the mine. Mining engineers have developed several ways of  
577 reducing water inflow in mine workings, however, creating a reduction procedure is difficult without knowing the  
578 exact locations of water pathways into the mining levels. In this study, we combine a near-surface S-wave velocity  
579 model of the area, computed from the SW present in the high-resolution 2D and 3D seismic surveys, with legacy 3D  
580 reflection seismic data, and information obtained from underground mine mapping and drilling to (1) characterize and  
581 better understand near-surface lithological variations, and (2) enhance the imaging and delineation of faults and dykes  
582 that extend from the near-surface to the deeper mining levels, which may act as water preferential flow-pathways (Fig.  
583 15d). Generally, it is difficult to exactly determine which faults and dykes act as water preferential flow-pathways,  
584 however the dykes integrated in this study have been confirmed through underground mapping to be water-bearing.  
585 The results obtained in Figure 14 demonstrate that incorporating a near-surface S-wave velocity model along with  
586 deeper P-wave seismic reflection models, mining level mapping, and drilling information enables a more  
587 comprehensive, accurate, and reliable understanding of the subsurface environment to be drawn. In the case of South  
588 Deep Gold Mine, it allowed for possible water preferential flow-pathways linking the Chuniespoort Group dolomites  
589 with the deeper situated mining level to be delineated with more certainty. From the tectonic point of view, the near-  
590 surface S-wave velocity models show that these dykes possibly cross-cut the entire stratigraphy including the  
591 Transvaal Supergroup, indicating that these dykes were active post the deposition of the supergroup. The observation  
592 indicates that these dykes are associated with pre-, syn-, and post-Bushveld deformation events and are likely  
593 associated with intrusion events such as the Bushveld Complex, Pilanesberg Complex, and Umkondo Large Igneous  
594 Province (Hartzer, 1989; Du Plessis and Walraven, 1990; Hartzer, 1995).

595

596 **6 Conclusion**

597 Surface wave analysis, conducted on DSR surveys using MASW, was used to investigate the near-surface (top 300  
598 m) in the vicinity of South Deep Gold Mine (South Africa) and investigate the effectiveness of integrating a near-  
599 surface S-wave velocity model with a deep reflection seismic reflection data, mine mapping, and drilling information  
600 to aid in delineating possible water preferential flow-pathways. To improve the robustness and spectral resolution of  
601 the dispersion images and thus of the S-wave velocity imaging, we were compelled to use large spatial windows to

602 process the data. Additionally, to improve the data coverage and subsurface mapping in the study area, we utilize the  
603 reciprocity principle to increase the data density in areas where no receiver locations, but source locations, were  
604 present.

605 The attained near-surface S-wave velocity models revealed the occurrence of sheet-like layering, and the presence of  
606 a S-wave velocity reversal zone, marking the contact between the Hekpoort and Timeball Hill Formations constituting  
607 the upper formations in the study area, respectively. The S-wave velocity analysis also revealed the occurrence of  
608 intrusive dykes, dip- and slump-faulting, which are all geological features characteristic of the West Rand Goldfield.  
609 As the mine is to be extended in the near future, the near-surface results obtained in this research reveal the need for  
610 more detailed near-surface investigations to be conducted to avoid placing future mining infrastructure in areas where  
611 it may be compromised by prevalent geological features in the area, such as fractures, joints, and faults.

612 Integrating a near-surface velocity model with deeper P-wave seismic reflection data, mine mapping, and drilling  
613 information introduces a novel approach to delineating possible water preferential flow-pathways to deep mining  
614 levels and has proved to possess great potential for delineating water preferential flow-pathways and possible  
615 structures that may pose a risk for deep mining. Of significance is that the results obtained in the study reveal that  
616 there is value in conducting SW analysis on DSR exploration survey data. They show that complexities that cannot  
617 be resolved by single techniques due to intrinsic limitations such as investigation depth, subsurface complexity, and  
618 velocity inversion ambiguities can be better handled by integrating shallow and deep subsurface velocity models and  
619 ground truth data.

620

621 *Author Contributions.* MSDM came up with the study idea, obtained funding, co-designed the seismic surveys, and  
622 guided the manuscript preparation and write-up. LVS co-developed the manuscript concept, provided guidance on  
623 data processing, and manuscript preparation. FKA designed the layered model used for surface wave processing,  
624 processed the 2D surface wave profiles, and reviewed the manuscript. CC conducted the data preparation for  
625 processing and provided valuable input in the data processing workflow. MK initiated the 3D processing and reviewed  
626 the manuscript. JA assisted with the manuscript preparation (discussion write-up) and interpretation. SG carried out  
627 the 3D processing, data integration, and manuscript writing. MSDM, LVS, and JB contributed significantly to the  
628 overall data integration, interpretation, and processing.

629

630 *Conflict of interest.* The authors declare that they have no conflict of interest.

631

632 *Acknowledgements.* This research was funded by the FUTURE project (Fiber-optic sensing and UAV-platform  
633 techniques for innovative mineral exploration) of the ERA-NET Cofound on Raw Materials (ERA-MIN3), Advanced  
634 Orebody Knowledge (AOK), Vinnova (Sweden), Ministry of Universities and Research (Italy), National Agency for  
635 Research (France), and DSI-NRF Centre of Excellence (CoE) for Integrated Mineral and Energy Resource Analysis

636 (CIMERA). Much gratitude goes to the Department of Science and Innovation (DSI) for funding the South African  
637 partners in the FUTURE project. We would like to extend our gratitude to South Deep Gold Mine of Gold Fields Ltd.  
638 for granting us access to their mine, permission to conduct research and publish the outcome of the research. We also  
639 wish to extend our gratitude to Smart Seismic Solutions (S<sup>3</sup>) for the acquisition of the 2023 2D and 3D reflection  
640 seismic surveys. Researchers and postgraduate students from the Wits Seismic Research Centre at the University of  
641 the Witwatersrand, Politecnico di Torino, Uppsala University, and Venda University are also greatly acknowledged  
642 for their contributions to the success of the ERA-MIN3- FUTURE project.

643

644

645

646

647

648

649

650

651

652

653

654

655

656

657

658

659

660

661

662

663

664 **References**

- 665 Auken, E., and Christiansen, A.V.: Layered and laterally constrained 2D inversion of resistivity data. *Geophysics*,  
666 69(3), 752-61, 2004.
- 667 Bekker, A., Planavsky, N., Rasmussen, B., Krapez, B., Hofmann, A., Slack, J., Rouxel, O., and Konhauser, K.: Iron  
668 formations: Their origins and implications for ancient seawater chemistry. In *Treatise on geochemistry*  
669 (Elsevier), 12, 561–628, 2014.
- 670 Boiero, D., and L.V. Socco.: Retrieving lateral variations from surface wave dispersion curve analysis: *Geophysical*  
671 *Prospecting*, 58, 977-996, 2010.
- 672 Burger, A.J., and Coertze, F.J.: Radiometric age determinations on rocks from southern Africa up to the end of 1971.  
673 *Bulletin Geological Society South Africa*, 58, 1-46, 1973.
- 674 Button, A., and Cawthorn, R.G.: Distribution of mafic sills in the Transvaal Supergroup, northeastern South  
675 Africa. *Journal of the Geological Society*, 172(3), 357-367, 2015.
- 676 Campbell, G., and Crotty, J.H.: 3-D seismic mapping for mine planning purposes at the South Deep prospect. In:  
677 Ross-Watt, D.A.J., Robinson, P.D.K. (Eds.), *Proceedings International Deep Mining Conference*. SAIMM  
678 *Symposium Series*, S10, 2, 569–597, 1990.
- 679 Campbell, G., and Crotty, J.H.: The application of 3-D seismic surveys to mine planning. *South African Chamber of*  
680 *Mines MINTEK*, Seminar, 1988.
- 681 Claerbout, J.F., and Green, I.: *Basic earth imaging*. Stanford University, Stanford, 2008.
- 682 Cousins, C.A.: The stratigraphy, structure and igneous rocks of the Transvaal System at the Western Areas Gold  
683 Mine. *South African Journal of Geology*, 65(2), 13-40, 1962.
- 684 Coward, M.P., 1995. Structural and tectonic setting of the Permo-Triassic basins of northwest Europe. *Geological*  
685 *Society, London, Special Publications*, 91(1), 7-39, 1995.
- 686 Dorland, H.C.: Provenance ages and timing of sedimentation of selected neoproterozoic and paleoproterozoic successions  
687 on the Kaapvaal Craton. Unpublished Ph.D. thesis, Rand Afrikaans University, Johannesburg, South Africa,  
688 326, 2004.
- 689 Du Plessis, C.P., and Walraven, F.: The tectonic setting of the Bushveld complex in Southern Africa, part 1: structural  
690 deformation and distribution. *Tectonophysics*, 179 (3–4), 305–319, 1990.
- 691 Eaton, D.W., Milkereit, B., and Salisbury, M.H.: Hardrock seismic exploration. *Society of Exploration Geophysicists*,  
692 1-6, 2003.
- 693 Eriksson, P.G., Schweitzer, J.K., Bosch, P.J.A., Schreiber, U.M., Van Deventer, J.L., and Hatton, C.J.: The Transvaal  
694 sequence: an overview. *Journal of African Earth Sciences (and the Middle East)*, 16(1-2), 25-51, 1993b.

- 695 Evans, B.J., Urosevic, M., and Cocker, J.: The use of seismic methods for the detection of dykes, 1998.
- 696 Foti, S., Lai, C.G., and Lancellotta, R.: Porosity of fluid-saturated porous media from measured seismic wave  
697 velocities. *Géotechnique*, 52(5), 359-373, 2002.
- 698 Franchi, F.: Petrographic and geochemical characterization of the Lower Transvaal Supergroup stromatolitic  
699 dolostones (Kanye Basin, Botswana). *Precambrian Research*, 310, 93-113, 2018.
- 700 Frimmel, H.E., and Nwaila, G.T.: Geologic evidence of syngenetic gold in the Witwatersrand Goldfields, South  
701 Africa, 2020.
- 702 Frimmel, H.E.: A giant Mesoarchean crustal gold-enrichment episode.: Possible causes and consequences for  
703 exploration. In: Kelley, K., Golden, H.C (Eds.) *Building Exploration Capability for the 21<sup>st</sup> Century*. Society  
704 of Economic Geologists, Special Publication, 209-234, 2014.
- 705 Frimmel, H.E.: The Witwatersrand Basin and Its Gold Deposits. In: Kröner, A., Hofmann, A. (eds) *The Archaean  
706 Geology of the Kaapvaal Craton, Southern Africa*. Regional Geology Reviews. Springer, 2019.
- 707 Gibson, M.A.S.: Interpretation of the 2003 South Deep 3D seismic survey. Unpublished internal report to Gold Fields  
708 Mining, 62, 2005.
- 709 Grandjean, G., and Bitri, A.: 2M-SASW: Multifold multichannel seismic inversion of local dispersion of Rayleigh  
710 waves in laterally heterogeneous subsurfaces: application to the Super-Sauze earthflow, France. *Near Surface  
711 Geophysics*, 4(6), 367-375, 2006.
- 712 Groves, P., Cascante, G., Dundas, D., and Chatterji, P.K.: Use of geophysical methods for soil profile  
713 evaluation. *Canadian Geotechnical Journal*, 48(9), 1364-1377, 2011.
- 714 Graczyk, A., Malinowski M., and Bellefleur, G.: Enhancing 3D post-stack seismic data acquired in hardrock  
715 environment using 2D curvelet transform. *Geophysical Prospecting* 63, 903–918, 2015.
- 716 Hartzer, F.J.: Stratigraphy, structure, and tectonic evolution of the crocodile river fragment. *South African Journal of  
717 Geology*. 92 (2), 110–124, 1989.
- 718 Hartzer, F.J.: Transvaal Supergroup inliers: geology, tectonic development and relationship with the Bushveld  
719 complex, South Africa. *Journal of African Earth Sciences*, 21 (4), 521–547, 1995.
- 720 Heinonen S., Kukkonen I., Heikkinen P., and Schmitt D.: High resolution reflection seismics integrated with deep  
721 drill hole data in Outokumpu, Finland. *Geological Survey of Finland, Special Paper* 51, 105–118, 2011.
- 722 Katou, M., Abe, S., Saito H., and Sato, H.: Reciprocal data acquisition and subsequent waveform matching for  
723 integrated onshore-offshore seismic profiling. *Geophysical Journal International*, 212, 509-521, 2017.

- 724 Khosro Anjom, F., Adler, F., and Socco, L.V.: Comparison of surface-wave techniques to estimate S-and P-wave  
725 velocity models from active seismic data. *Solid Earth*, 15(3), 367-386, 2024.
- 726 Killick, A.M.: Pseudotachylites of the West Rand Goldfield, Witwatersrand Basin, South Africa, Doctor of Philosophy  
727 Thesis, Rand Afrikaans University, Johannesburg South Africa. 18, 1992.
- 728 Knopoff, L., and Gangi, A. F.: Seismic reciprocity: *Geophysics*, 24, 681–691, 1959.
- 729 Kositcin, N., and Krapež, B.: Relationship between detrital zircon age-spectra and the tectonic evolution of the Late  
730 Archaean Witwatersrand Basin, South Africa. *Precambrian Research*, 129(1-2), 141-168, 2004.
- 731 Laake, A., Strobbia, C., and Cutts, A.: Integrated approach to 3D near surface characterization in desert regions. first  
732 break, 26(11), 2008.
- 733 Lin, C.P., Lin, C.H., and Chien, C.J.: Dispersion analysis of surface wave testing–SASW vs. MASW. *Journal of*  
734 *Applied Geophysics*, 143, 223-230, 2017.
- 735 Malehmir, A., Koivisto, E., Manzi, M., Cheraghi, S., Durrheim, R.J., Bellefleur, G., Wijns, C., Hein, K.A., and King,  
736 N.: A review of reflection seismic investigations in three major metallogenic regions: The Kevitsa Ni–Cu–  
737 PGE district (Finland), Witwatersrand goldfields (South Africa), and the Bathurst Mining Camp  
738 (Canada). *Ore Geology Reviews*, 56, 423-441, 2014.
- 739 Malehmir, A., Maries, G., Bäckström, E., Schön, M., and Marsden, P.: Developing cost-effective seismic mineral  
740 exploration methods using a landstreamer and a drophammer. *Scientific Reports*, 7(1), 10325, 2017.
- 741 Malehmir, A., Wang, S., Lamminen, J., Brodic, B., Bastani, M., Vaitinen, K., Juhlin, C., and Place, J.: Delineating  
742 structures controlling sandstone-hosted base-metal deposits using high-resolution multicomponent seismic  
743 and radio-magnetotelluric methods: a case study from Northern Sweden. *Geophysical Prospecting*, 63(4),  
744 774-797, 2015.
- 745 Manzi, M.S., Durrheim, R.J., Hein, K.A., and King, N.: 3D edge detection seismic attributes used to map potential  
746 conduits for water and methane in deep gold mines in the Witwatersrand basin, South  
747 Africa. *Geophysics*, 77(5), WC133-WC147, 2012a.
- 748 Manzi, M.S., Gibson, M.A., Hein, K.A., King, N., and Durrheim, R.J.: Application of 3D seismic techniques to  
749 evaluate ore resources in the West Wits Line goldfield and portions of the West Rand goldfield, South  
750 Africa. *Geophysics*, 77(5), WC163-WC171, 2012b.
- 751 Manzi, M.S., Hein, K.A., King, N., and Durrheim, R.J.: Neoarchaean tectonic history of the Witwatersrand Basin and  
752 Ventersdorp Supergroup: New constraints from high-resolution 3D seismic reflection  
753 data. *Tectonophysics*, 590, 94-105, 2013a.

- 754 Manzi, M.S., Hein, K.A.A., Durrheim, R., and King, N.: Seismic attribute analysis to enhance detection of thin gold-  
755 bearing reefs: South Deep gold mine, Witwatersrand basin, South Africa. *Journal of Applied Geophysics*, 98,  
756 212-228, 2013b.
- 757 Martin, D.M., Clendenin, C.W., Krapez, B., and McNaughton, N.J.: Tectonic and geochronological constraints on late  
758 Archaean and Palaeoproterozoic stratigraphic correlation within and between the Kaapvaal and Pilbara  
759 Cratons. *Journal of the Geological Society*, 155(2), 311-322, 1998.
- 760 Masethe, R.T., Manzi, M.S., and Durrheim, R.J.: Using legacy 3D seismic data and source parameters of mining-  
761 induced earthquakes to mitigate the risk of rockbursting in Kloof Gold Mine, South Africa. *Geophysical*  
762 *Prospecting*, 71(7 Special Issue: Mineral Exploration and Mining Geophysics), 1281-1311, 2023.
- 763 McCarthy, T.S.: The Witwatersrand Supergroup. *The Geology of South Africa*. Geological Society of South Africa,  
764 2006.
- 765 Mutshafa, N., Manzi, M.S., Westgate, M., James, I., Brodic, B., Bourdeau, J.E., Durrheim, R.J., and Linzer, L.:  
766 Seismic imaging of the gold deposit and geological structures through reprocessing of legacy seismic profiles  
767 near Kloof–Driefontein Complex East Mine, South Africa. *Geophysical Prospecting*, 71(7 Special Issue:  
768 Mineral Exploration and Mining Geophysics), 1181-1196, 2023.
- 769 Neducza, B.: Stacking of surface waves. *Geophysics*, 72(2), V51-V58, 2007.
- 770 Nwaila, G.T., Frimmel, H.E., Zhang, S.E., Bourdeau, J.E., Tolmay, L.C., Durrheim, R.J., and Ghorbani, Y.: The  
771 minerals industry in the era of digital transition: An energy-efficient and environmentally conscious  
772 approach. *Resources Policy*, 78, 102851, (2022).
- 773 Nwaila, G.T., Ghorbani, Y., Becker, M., Frimmel, H.E., Petersen, J., and Zhang, S.: Geometallurgical approach for  
774 implications of ore blending on cyanide leaching and adsorption behavior of Witwatersrand gold ores, South  
775 Africa. *Natural Resources Research*, 29(2), 1007-1030, 2020a.
- 776 Osburn, K., Pretorius, H., Kock, D., King, N., Pillaye, R., and Hlangwane, M.: Enhanced geological modelling of the  
777 Upper Elsburg reefs and VCR to optimize mechanized mine planning at South Deep Gold Mine. *Journal of*  
778 *the Southern African Institute of Mining and Metallurgy*, 114(3), 265-273, 2014.
- 779 Papadopoulou, M., Da Col, F., Mi, B., Bäckström, E., Marsden, P., Brodic, B., Malehmir, A., and Socco, L.V.:  
780 Surface-wave analysis for static corrections in mineral exploration: A case study from central  
781 Sweden. *Geophysical Prospecting*, 68, 214-231, 2020.
- 782 Park, C.B., Miller, R.D., and Xia, J.: Imaging dispersion curves of surface waves on multi-channel record. In *Society*  
783 *of Exploration Geophysicists technical program expanded abstracts 1998*, 1377-1380, 1998.
- 784 Parsons, C.F., and Killick, A.M.: A reassessment of the structure of the dolomite inliers southeast of Westonia. *South*  
785 *African journal of geology*, 93(3), 438-442, 1990.

- 786 Pegah, E., and Liu, H.: Application of near-surface seismic refraction tomography and multichannel analysis of surface  
787 waves for geotechnical site characterizations: A case study. *Engineering Geology*, 208, 100-113, 2016.
- 788 Pileggi, D., Rossi, D., Lunedei, E., and Albarello, D.: Seismic characterization of rigid sites in the ITACA database  
789 by ambient vibration monitoring and geological surveys. *Bulletin of Earthquake Engineering*, 9, 1839-1854,  
790 2011.
- 791 Pretorius, C.C., Jamison, A.A., and Irons, C.: Seismic exploration in the Witwatersrand Basin, Republic of South  
792 Africa. In *Proceedings of Exploration '87*, ed. Garland, G.D. Ontario Geological Survey. 3, 241–253, 1989.
- 793 Rapetsoa, M.K., Manzi, M.S.D., Sihoyiya, M., Malehmir, A., James, I., Socco, L.V., Lepine, J., Colombero, C.,  
794 Valeshin, O., and Durrheim, R.J.: Advanced seismic acquisition techniques in South African mines: Insights  
795 from the FUTURE project. *Journal of the Southern African Institute of Mining and Metallurgy*, 125(1), 25-  
796 32, 2025.
- 797 Saunders S., Lamb P., and Sweeney D.: High resolution seismic for resolving coal seam structure in difficult terrain.  
798 *Geophysics* 22, 325–332, 1991.
- 799 Sheriff, R.E.: *Encyclopedic dictionary of applied geophysics*, 4th ed. Society of Exploration Geophysicists, Tulsa,  
800 2002.
- 801 Smith, A.J., and Beukes, N.J.: Palaeoproterozoic Banded Iron formationhosted High-Grade Hematite Iron Ore  
802 Deposits of the Transvaal Supergroup, South Africa. *Episodes*, 39(2), 269–284, 2016.
- 803 Socco L.V., Comina, C., and Khosro Anjom, F.: Time-average velocity estimation through surface-wave analysis:  
804 Part 1 — S-wave velocity: *Geophysics*, 82(3), U49–U59, 2017.
- 805 Socco, L.V., and Strobbia, C.: Surface-wave method for near-surface characterization: A tutorial: *Near Surface*  
806 *Geophysics*, 2, 165–185, 2004.
- 807 Socco, L.V., Boiero, D., Foti, S., and Wisén, R.: Laterally constrained inversion of ground roll from seismic reflection  
808 records. *Geophysics*, 74(6), G35-G45, 2009.
- 809 Socco, L.V., Foti, S., and Boiero, D.: Surface-wave analysis for building near-surface velocity models—Established  
810 approaches and new perspectives. *Geophysics*, 75(5), 75A83-75A102, 2010.
- 811 Socco, L.V., Papadopoulou, M., Federico, D.C., Chiara, C., Emma, B., Paul, M., and Alireza, M.: Surface wave  
812 dispersion analysis in hard rock sites: challenges and opportunities. In *Geophysical Research Abstracts*, 21,  
813 2019.
- 814 Strong, S.: Modelling complex near-surface features to improve shallow seismic exploration. *ASEG Extended*  
815 *Abstracts*, 2018(1), 1-4, 2018.

- 816 Urosevic, M., Sherlock, D., Kepic, A., and Dodds, K.: 2007. Land seismic acquisition repeatability for time-lapse  
817 monitoring of CO2 sequestration. ASEG Extended Abstracts, 2007(1), 1-1, 2007.
- 818 Van Niekerk, H.J., and Van der Walt, I.J.: Dewatering of the Far West Rand dolomitic area by gold mining activities  
819 and subsequent ground instability. Land Degradation & Development, 17(4), 441-452, 2006.
- 820 Veevers, J.J.: Morphotectonics of rifted continental margins in embryo (East Africa), youth (Africa-Arabia), and  
821 maturity (Australia). The Journal of Geology, 89(1), 57-82, 1981.
- 822 Vermaakt, D.T., Chunnet, I.E., and Anhaeusser, C.R.: Tectono-sedimentary processes which controlled the deposition  
823 of the Ventersdorp Contact Reef within the West Wits Line. In Proceedings of the 15th Congress of the  
824 Council for Mining and Metallurgical Institutions, South African Institute of Mining and Metallurgy, (3),  
825 117-130, 1994.
- 826 Wilczynski, Z., Kaslilar, A., Malehmir, A., Manzi, M., Vivin, L., Lepine, J., Valishin, O., and Högdahl, K.: Ambient  
827 noise surface-wave imaging in a hardrock environment: implications for mineral exploration. Geophysical  
828 Journal International, 240(1), 571-590, 2025.
- 829 Wisén, R., and Christiansen, A.V.: Laterally and mutually constrained inversion of surface wave seismic data and  
830 resistivity data. Journal of Environmental & Engineering Geophysics, 10(3), 251-262, 2005.
- 831 Wolmarans, J.F.: Ontwatering van die dolomietgebied aan die verre Wes-Rand: gebeure in perspektief. University of  
832 Pretoria (South Africa), 1984.
- 833 Zhou, B., Hatherly, P., Peters, T., and Sun, W.: Experience with the issue of seismic surveying over basalts. ASEG  
834 Extended Abstracts, 1-5, 2010.
- 835 Zhu, X., Valasek, P., Roy, B., Shaw, S., Howell, J., Whitney, S., Whitmore, N.D., and Anno, P.: Recent applications  
836 of turning-ray tomography. Geophysics, 73(5), VE243-VE254, 2008.
- 837
- 838